Robotica (2016) volume 34, pp. 71–97. © Cambridge University Press 2014
doi:10.1017/S0263574714001398

Approximate analytical solution for vibration of a 3-PRP planar parallel robot with flexible moving platform

Mahdi Sharifnia* and Alireza Akbarzadeh

Mechanical Engineering Department, Center of Excellence on Soft Computing and Intelligent Information Processing (SCIIP), Ferdowsi University of Mashhad, Mashhad, Iran

(Accepted May 2, 2014. First published online: June 13, 2014)

SUMMARY

In this research, using an approximate analytical method, vibration analysis of a 3-PRP (active prismatic—P, passive revolute—R, passive prismatic—P) planar parallel robot having a flexible moving platform is presented. A specific architecture of the 3-PRP parallel robot, also known as the ST (Star-Triangle) parallel robot, is considered. The moving platform of the robot, called the star, is assumed to be made of three flexible beams shaped like a star. For analytical modeling, each of the three beams of the star is assumed to be a discrete Euler–Bernoulli beam with a passive prismatic joint. Continuity equations at the center of the star are used to relate vibrations of the three beams. The vibration behavior of each beam is modeled using previously developed constrained motion equations for a planar Euler–Bernoulli beam having a prismatic joint. In this paper, previously presented "constrained assumed modes method" is further developed to solve the constrained motion equation for the ST parallel robot. The solution method is used to obtain the vibration of the robot for the inverse dynamics problem and simultaneously provides generalized constraint forces. Furthermore, the solution method can be used for the direct dynamics problem of the ST robot. Several input trajectories are considered to investigate the different behavior for the center of the star. For each of the trajectories, three different groups of mode shapes are considered and their vibrational responses are compared. In this research, for the first time, effects of the passive prismatic joint parameters such as mass, rotational moment of inertia, and its actual length are considered in an analytical model. Finally, the analytical solution and a FEM (Finite Element Method) software solution are compared.

KEYWORDS Parallel manipulator; Flexible; Prismatic joint; Time-variant constraint; Vibration; Assumed modes.

1. Introduction

The use of parallel robots continues to grow in industrial applications. Higher speed and higher accuracy as well as higher stiffness to weight ratio and strength to weight ratio are some of the reasons why parallel robots have found a wide spectrum of applications. Microsurgery, space robotics, maintenance of nuclear plants, and high-speed pick and place tasks represent some of the applications commonly used by the parallel robots. Because of the requirements for high-speed and high-acceleration, links of the parallel robots are constructed with lightweight materials which can result in undesirable vibration. In this research, we focus on vibration analysis of the parallel robots in which its moving platform is flexible and has passive prismatic joint(s). Specially, a 3-PRP (active prismatic—P, passive revolute—R, passive prismatic—P) parallel robot is the subject of this research.

Many researchers have studied and modeled dynamic motion of the flexible manipulators. Several methods are used such as assumed mode method (AMM), finite element method (FEM), and lumped parameter modeling. However, complicated geometries and multiple kinematic chains of

* Corresponding author. E-mail: sharifnia.mehdi@gmail.com

https://doi.org/10.1017/S0263574714001398 Published online by Cambridge University Press

the parallel robots result in complicated kinematics and dynamics analysis. Consequently, analytical or approximate analytical methods are less used for vibration analysis of flexible parallel robots. Many researchers have used FEM for deriving dynamic equations of motion and perform vibration analysis of flexible parallel robots. Fattah *et al.*[1,2] presented kinematics and dynamics of a 3-RRS spatial flexible parallel robot, respectively. They used finite elements for the discretization of the flexible links. Fattah *et al.*[3] performed a dynamic analysis of a flexible-link planar parallel manipulator in Cartesian space using FEM. Fattah *et al.*[1–3] use the potential energy of a beam element to include the effect of the flexibility of a "planar beam-shaped flexible links." Piras *et al.*[4] presented a dynamic analysis of a planar 3-PRR flexible parallel robot using FEM, and investigated effect of high-speed motion on the vibrations of the robot. In ref. [5], dynamic modeling of a flexible-link planar parallel platform is performed using a sub-structuring approach and the Lagrange finite element formulation are used to model flexible linkages. Zhaocai and Yueqing[6] present a method for dynamic modeling of flexible parallel robots with rigid moving platform using FEM. This reference uses kineto-elastodynamics theory and Timoshenko beam theory to derive the motion equations. In ref. [7], vibration analysis of a flexible 3-PRS parallel robot is presented using FEM. Shan-zeng *et al.*[8] modeled 3-RRS parallel robot and solved its dynamic equations using the Newmark numerical method.

Some researchers used analytical methods for vibration analysis of flexible parallel robots. Kang and Mills[9] and Zhang *et al.*[10] presented a linearized analytical model for a planar 3-PRR flexible parallel robot using AMM. Lagrange's multipliers are used in their dynamic equations. Giovagnoni[11] used the principle of virtual work and presented a general method for dynamic analysis of flexible closed-chain manipulators. Lee and Geng[12] presented a dynamic model for a flexible Stewart parallel robot. Dwivedy and Eberhard[13] presented a literature review for dynamic modeling of flexible manipulators. In addition to dynamic modeling, many researchers have presented vibration control of flexible parallel robots. For example, Kang and Mills[9] and Zhang *et al.*[10] performed active vibration control for a planar 3-PRR flexible parallel robot using PZT (piezoelectric) actuators.

In general, vibration analysis of flexible parallel robots with prismatic joints is relatively complicated as the passive prismatic joints result in time-varying boundary conditions or holonomic constraints on the flexible links. To the best of the author's knowledge, aside from a few FEM studies, there exists only one approximate analytical study on vibration analysis of flexible parallel robots with passive prismatic joints.[14] Authors of the present paper have presented a motion equation in variational form for vibration of an Euler–Bernoulli beam having a passive prismatic joint.[14] The flexible beam is used as a moving platform for a PR-PRP parallel robot. In refs. [14] and [15], solution of the motion equation is performed using a constrained assumed modes method. In traditional assumed modes method, each of the assumed mode shapes must satisfy all the geometrical boundary conditions. However, using the constrained assumed modes method, the assumed mode shapes each satisfy only time-invariant boundary conditions and do not satisfy time-variant geometrical boundary conditions. Instead, by writing additional time-variant constraint equations, the combination of the assumed modes will satisfy the time-variant geometrical boundary conditions. Ibrahimbegovic and Mamouri[16] presented a discussion about finite element implementation of internal holonomic constraints in a beam model. Constraint relationships are written for revolute and prismatic joints. Bauchau[17] performed modeling of prismatic joints for flexible multi-body systems using FEM. Ibrahimbegovic and Mamouri[16] and Bauchau[17] use the finite element method and beam element. Including the passive prismatic joint parameters such as mass, moment of inertia, and its actual length increases the challenges for dynamic modeling of the flexible parallel robots. Stoenescu and Marghitu[18] investigated rigid planar kinematic chains and showed that the moment of inertia effect for prismatic joints can be significant at high speeds. The dynamic effect of the passive prismatic joint length is investigated on the vibration response for the PR-PRP parallel robot.[14]

Dynamic modeling, vibration analysis, and control of flexible-link manipulators are still open fields for recent researches. In ref. [21], each flexible link is modeled as a six-dimensional generalized spring (concept of generalized spring). In ref. [22], a novel method for dynamic modeling of 3-D robots with large displacements and small elastic deformations is developed by means of an Equivalent Rigid Link System (ERLS) approach.[22] Mosayebi *et al.*[23] and Staufer and Gattringer[24] present methods to estimate the state of the elastic degrees of freedom for flexible-link manipulators.

Considering the existing body of literature on flexible parallel manipulators, it may be concluded that:

https://doi.org/10.1017/S0263574714001398 Published online by Cambridge University Press

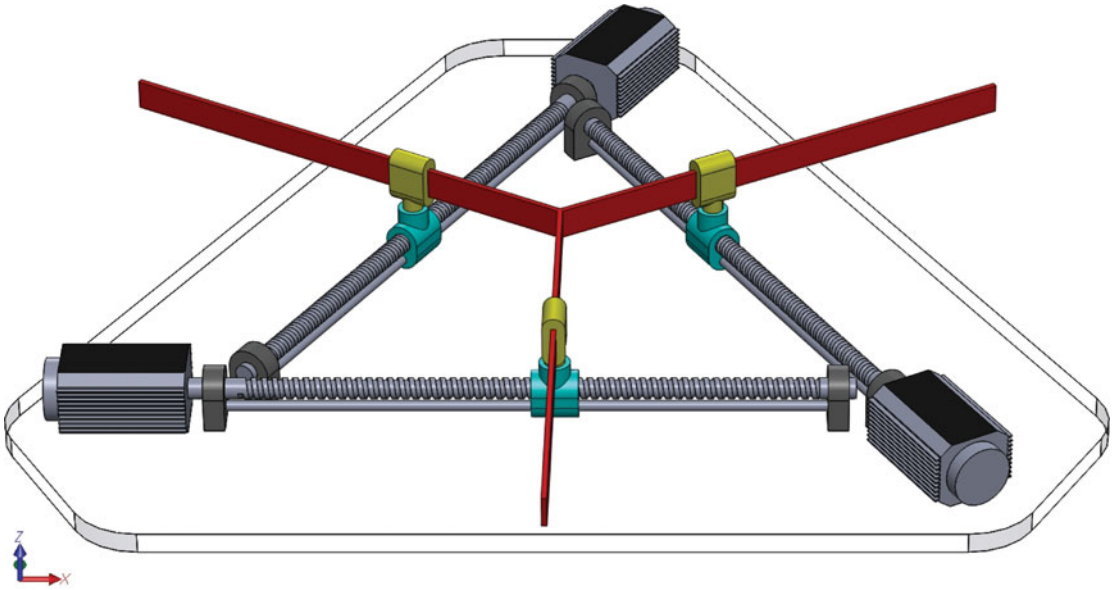


Fig. 1. The 3-PRP parallel robot or ST (Star-Triangle).

1. Analytical methods are less used and most researchers used FEM or other numerical methods for the vibration solution of parallel robots.
2. There are few FEM existing studies on flexible parallel robots with prismatic joints. There is only one existing approximate analytical study where the moving platform is flexible and has passive prismatic joint.
3. The effect of mass, moment of inertia, and actual length of the prismatic joint on the vibration response is not considered in analytical methods.

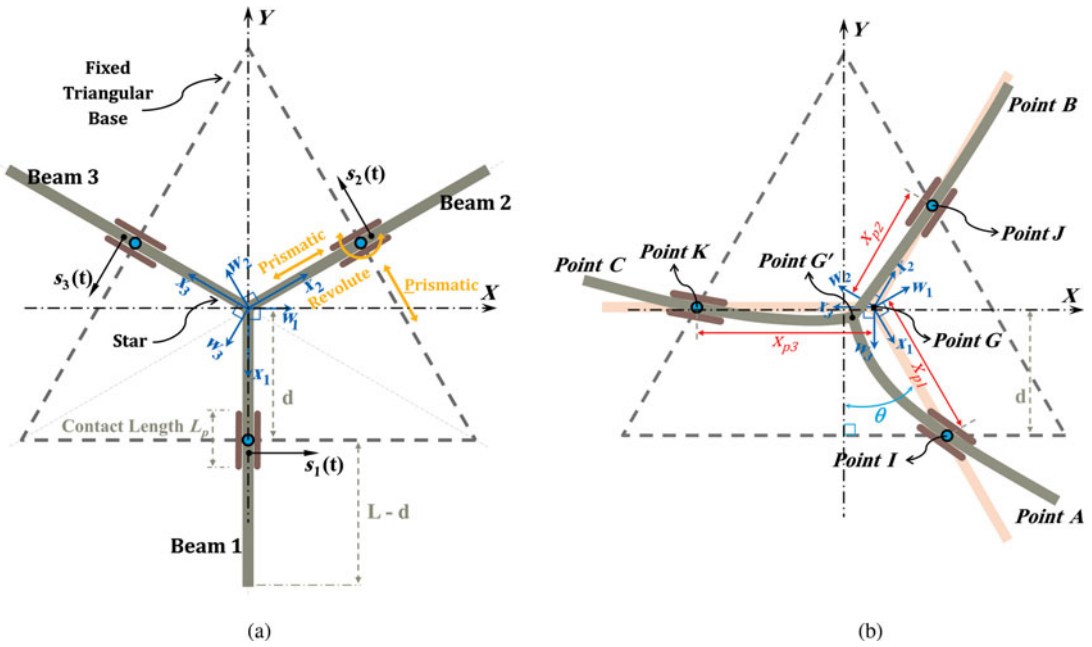
The present study aims to offer certain advantages for each of the above three shortcomings. To do this, a 3-PRP parallel robot with a flexible moving platform and passive prismatic joints is considered. The 3-PRP parallel robot presented in this research has three symmetric closed-loop chains. Each chain consists of an active prismatic joint (P), a passive revolute joint (R), and a passive prismatic joint (P).

The rest of this paper is organized as follows. In Section 2, robot structure is introduced. In Section 3, kinematics of the robot is presented. In Section 4, constraint equations for the center of the moving star is developed. In Section 5, effect of vibration of the moving platform on axial acceleration of the beams is investigated. In Section 6, motion equations are developed and the motion constraints are incorporated into the motion equation. In Section 7, an approximate analytical solution for the motion equations using the "constrained assumed modes method" is presented. In Section 8, numerical results of four case studies are presented. In Section 9, a discussion about mode shape selection and its effect on the correctness and accuracy of the approximate analytical solution is presented. In Section 10, concluding remarks are presented.

2. Robot Structure

There are two main types of planar 3-PRP parallel robots. The first 3-PRP parallel robot is known as DT (double-triangle).[19] The moving platform of this type is made of three beams formed like a triangle. The second planar 3-PRP parallel robot is known as ST (star-triangle) and is shown in Fig. 1.[20] This robot can be used for machining mechanisms because of its positioning accuracy and resolution capability; see ref. [20]. The planar 3-PRP parallel robot has three degrees of freedom. The subject of the present investigation is the ST parallel robot. The ST parallel robot has three active prismatic joints which slide on its rigid triangular base. In the structure shown in Fig. 1, three motors drive the three active prismatic joints using three ball screw rods mounted on the triangular base. The moving platform of the robot is made of three beams formed like a star. It is assumed that the

https://doi.org/10.1017/S0263574714001398 Published online by Cambridge University Press



(a) (b)

Fig. 2. (a) General model of the ST robot with fixed XY and rigid body coordinate systems at time = 0; (b) The ST robot at a deformed position.

three beams are flexible. Therefore, the moving platform of this robot is flexible. Additionally, it is assumed that the three beams have the same physical and geometrical properties. The angle between each two branches of the star is assumed to be 120°. Each of the three beams is joined to the rigid triangular base using a group of PRP joints. Finally, the rigid base is assumed to be an equilateral triangle.

A general model of the ST robot in its start configuration is shown in Fig. 2(a). At the start of motion, the robot has no deformation. Center of the moving star and the center of the fixed triangular base coincide. Each of the three beams of the moving star intersects the corresponding side of the fixed base at its midpoint.

To obtain an analytical model for vibration analysis, the three branches of the moving platform are considered. The three branches, also referred to as beams 1, 2, and 3, are each modeled as a discrete Euler–Bernoulli beam with a prismatic joint. For beams 1, 2, and 3, a rigid body coordinate system is considered as x_1w_1, x_2w_2, and x_3w_3, respectively. See Figs. 2(a) and 2(b). The three rigid body coordinate systems are each attached to the rigid configuration of the corresponding beam. Center of the moving star at its rigid and deformed configurations are called G and G', respectively. Origins of the three coordinate systems are located at point G. The direction of each x-axis is along its corresponding rigid beam and passes through its revolute joint. Additionally, as shown in Fig. 2, a fixed coordinate system, XY with its origin O at the center of the equilateral triangle is defined.

In this paper, in order to focus on off-load behavior of the robot's working point, point G, it is assumed that the end effector has zero concentrated inertia and experiences zero external load. As stated earlier, each branch of the moving platform is assumed to be an Euler–Bernoulli beam. Therefore, the effects of the shear deformation and the rotational inertia moment are not considered in the motion equation of the beam element. Additionally, the magnitude and slope angle of the beam deformation are assumed to be small.

3. The ST Robot Kinematics

To perform vibration analysis for the ST robot, an analytical motion equation is written for an assumed element of the flexible moving platform. The acceleration term of the assumed element in the motion equation contains both rigid and flexible body accelerations. It is the rigid body motion that induces the flexible body motion. Due to geometric conditions and control strategies for a given motion,

https://doi.org/10.1017/S0263574714001398 Published online by Cambridge University Press

inverse or direct kinematics can be employed for its acceleration analysis needed in dynamics and control. In this research, it is assumed that input trajectories of the active joints can be obtained without any significant error by the motor drive system and therefore vibration of the ST robot at points I, J, and K are assumed to be zero. Consequently, by specifying input trajectories $s_1(t)$, $s_2(t)$, and $s_3(t)$ that represent the motion of the three actuated prismatic joints, the rigid body motion can be obtained using direct dynamics. By supplying the rigid body motion to the motion equation, the flexible body motion is obtained.

In this section, rigid acceleration of the element is obtained by specifying the three actuated prismatic joint trajectories $s_1(t)$, $s_2(t)$, and $s_3(t)$. To do this, the direct kinematics of the ST robot must be solved. In the direct kinematics problem, trajectories of the actuated prismatic joints are specified and position trajectory of point G as well as the orientation trajectory of the moving star is determined. Consider Figs. 2(a) and 3. Center of the rigid moving star, point G, represents the working point or where the end-effector is attached to the robot. Given the actuated joint trajectories, positions of the revolute joints, i.e. points I, J, and K on the fixed triangular base are determined. Position vectors of these points in the fixed coordinate system, XY are as follows:

$$\overrightarrow{OI} = \begin{bmatrix} s_1(t) \\ -d \end{bmatrix}, \tag{1}$$

$$\overrightarrow{OJ} = \begin{bmatrix} d\cos(\pi/6) - s_2(t)\sin(\pi/6) \\ d\sin(\pi/6) + s_2(t)\cos(\pi/6) \end{bmatrix}, \tag{2}$$

$$\overrightarrow{OK} = \begin{bmatrix} -d\cos(\pi/6) - s_3(t)\sin(\pi/6) \\ +d\sin(\pi/6) - s_3(t)\cos(\pi/6) \end{bmatrix}. \tag{3}$$

Having the positions of points I, J, and K, vectors $\overrightarrow{IJ}$, $\overrightarrow{JK}$, and $\overrightarrow{KI}$ can be written as

$$\begin{cases} \overrightarrow{IJ} = \overrightarrow{OJ} - \overrightarrow{OI} \\ \overrightarrow{JK} = \overrightarrow{OK} - \overrightarrow{OJ} \\ \overrightarrow{KI} = \overrightarrow{OI} - \overrightarrow{OK} \end{cases}. \tag{4}$$

Consider vectors $\overrightarrow{IJ}$, $\overrightarrow{JK}$, and $\overrightarrow{KI}$. The loci of point G such that each of $\angle IGJ$, $\angle JGK$, and $\angle KGI$ equals 120° are three arcs of three circles (Fig. 3). The cross section of any of these two arcs uniquely identifies the working point of the robot, point G. For example, by specifying the positions of points I, J and $\angle IGJ = 120°$, the position of point G will fall on circular arc $I\breve{G}J$. Additionally, by specifying positions of points J, K and of $\angle JGK = 120°$, the position of point G will also fall on circular arc $J\breve{G}K$. Therefore, intersection of these two arcs will yield the position of point G and insure that $\angle IGJ$ and $\angle JGK$ are both equal to 120°. Consequently, $\angle KGI$ will also equal to 120°. Radiuses of the mentioned arcs are obtained using the geometry of the central angle, inscribed angle, and triangle. For example in Fig. 3, consider the circle with center point C_{IJ}. Since the inscribed $\angle IGJ$ is equal to 120°, the central $\angle IC_{IJ}J$ in $\Delta IC_{IJ}J$ will also equal to 120°. Then, for the isosceles $\Delta IC_{IJ}J$, we have $|\overrightarrow{IC}_{IJ}| = (|\overrightarrow{IJ}|/2)/\sin(120°/2) = |\overrightarrow{IJ}|/\sqrt{3}$, or $R_{IJ} = |\overrightarrow{IJ}|/\sqrt{3}$. Therefore, for the circles with center points C_{IJ} and C_{JK}, we have

$$R_{IJ} = \left|\overrightarrow{IJ}\right|/\sqrt{3}, \quad R_{JK} = \left|\overrightarrow{JK}\right|/\sqrt{3}. \tag{5}$$

Position vectors for the arc centers containing the vectors $\overrightarrow{IJ}$ and $\overrightarrow{JK}$ can be written as

$$\begin{aligned} \overrightarrow{OC}_{IJ} &= \overrightarrow{OI} + \begin{bmatrix} \cos(-\pi/6) & -\sin(-\pi/6) \\ \sin(-\pi/6) & \cos(-\pi/6) \end{bmatrix} \overrightarrow{IJ}/\sqrt{3}, \\ \overrightarrow{OC}_{JK} &= \overrightarrow{OJ} + \begin{bmatrix} \cos(-\pi/6) & -\sin(-\pi/6) \\ \sin(-\pi/6) & \cos(-\pi/6) \end{bmatrix} \overrightarrow{JK}/\sqrt{3}. \end{aligned} \tag{6}$$

https://doi.org/10.1017/S0263574714001398 Published online by Cambridge University Press

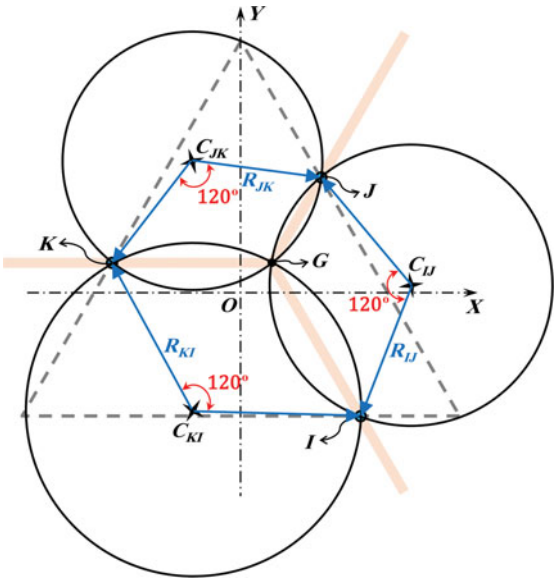


Fig. 3. Circles used to obtain point G.

Using the position of point G and the center of the circles, we can write

$$\begin{aligned} \left|\overrightarrow{OG} - \overrightarrow{OC}_{IJ}\right| &= R_{IJ}, \\ \left|\overrightarrow{OG} - \overrightarrow{OC}_{JK}\right| &= R_{JK}. \end{aligned} \tag{7}$$

By solving Eq. (7), the position vector $\overrightarrow{OG}$ is obtained. Then, by taking time derivative, acceleration of point G, a_G is obtained as

$$a_G = \frac{\mathrm{d}^2}{\mathrm{d}t^2}\left(\overrightarrow{OG}\right). \tag{8}$$

In Fig. 2(b), parameter θ represents the angular position, orientation of the moving star and is computed as follows:

$$\theta = \tan^{-1}\left(\frac{-1}{\text{slope}\left(\overrightarrow{GI}\right)}\right), \tag{9}$$

in which, slope($\overrightarrow{GI}$) represents slope of vector $\overrightarrow{GI}$. Therefore, using Eq. (9), at the start configuration of the robot, angle θ is zero. By taking the first and second time derivatives of Eq. (9), angular velocity and acceleration of rigid motion of the moving platform can be obtained. As shown in Fig. 2(b), length of vectors $\overrightarrow{GI}$, $\overrightarrow{GJ}$, and $\overrightarrow{GK}$ represent positions of the passive prismatic joints in the rigid body coordinate systems, x_1w_1, x_2w_2, and x_3w_3, as x_{p1}, x_{p2}, and x_{p3} respectively. Because the vibration amplitude and the slope angle of deformation are small, the distance between points G and G' is very small compared with the length of vectors $\overrightarrow{GI}$, $\overrightarrow{GJ}$, and $\overrightarrow{GK}$. Therefore, the lengths of vectors $\overrightarrow{G'I}$, $\overrightarrow{G'J}$, and $\overrightarrow{G'K}$ are assumed to be equal to the length of vectors $\overrightarrow{GI}$, $\overrightarrow{GJ}$, and $\overrightarrow{GK}$. Therefore,

$$x_{p1} = \left|\overrightarrow{GI}\right|, \quad x_{p2} = \left|\overrightarrow{GJ}\right|, \quad x_{p3} = \left|\overrightarrow{GK}\right|. \tag{10}$$

Upon obtaining rigid acceleration of point G, Eq. (8), the rigid acceleration of each point or element of the moving platform can be obtained. Consider an element on the beam number i, the rigid

https://doi.org/10.1017/S0263574714001398 Published online by Cambridge University Press

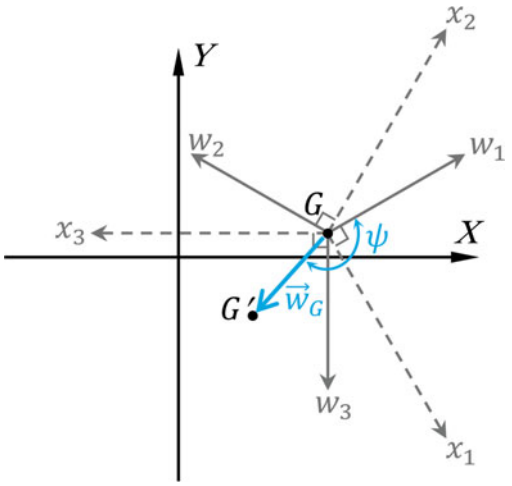


Fig. 4. Magnified view of the elastic displacement of point *G*.

acceleration components in directions x_i and w_i are a_{xi} and a_{wi} respectively. Therefore, we can write

$$a_{xi} = a_G.\hat{e}_{xi} - x_i\dot{\theta}^2, \quad \hat{e}_{xi} = \begin{bmatrix} \sin(\theta + (i-1)\,2\pi/3) \\ -\cos(\theta + (i-1)\,2\pi/3) \end{bmatrix} \quad i = 1, 2, 3, \tag{11}$$

$$a_{wi} = a_G.\hat{e}_{wi} + x_i\ddot{\theta}, \quad \hat{e}_{wi} = \begin{bmatrix} \cos(\theta + (i-1)\,2\pi/3) \\ \sin(\theta + (i-1)\,2\pi/3) \end{bmatrix} \quad i = 1, 2, 3, \tag{12}$$

in which $\hat{e}_{xi}$ and $\hat{e}_{wi}$ are the unit vectors in directions x_i and w_i respectively.

4. Constraint Equations for Center of the Moving Star

In Fig. 4, vector $\mathbf{w}_G$, representing elastic displacement of the center of the star, is shown in coordinate systems $x_i w_i$. Parameters w_G and ψ represent the norm of vector $\mathbf{w}_G$ and its angle with the w_1-axis, respectively. Required components are obtained by multiplying norm of vector $\mathbf{w}_G$ by cosine of its angle with x_i and w_i axes. If components of elastic displacement, w_G, in directions x_i and w_i are represented with x_{iG} and w_{iG} respectively, we can write

$$\left.\begin{aligned} x_{1G} &= w_G\cos\left(\tfrac{0\pi}{3} + \psi - \tfrac{\pi}{2}\right) \\ x_{2G} &= w_G\cos\left(\tfrac{2\pi}{3} + \psi - \tfrac{\pi}{2}\right) \\ x_{3G} &= w_G\cos\left(\tfrac{4\pi}{3} + \psi - \tfrac{\pi}{2}\right) \end{aligned}\right\} \Rightarrow x_{iG} = w_G\sin\left(\frac{2\pi}{3}(i-1) + \psi\right), \quad i = 1, 2, 3, \tag{13}$$

$$\left.\begin{aligned} w_{1G} &= w_G\cos\left(\tfrac{0\pi}{3} + \psi\right) \\ w_{2G} &= w_G\cos\left(\tfrac{2\pi}{3} + \psi\right) \\ w_{3G} &= w_G\cos\left(\tfrac{4\pi}{3} + \psi\right) \end{aligned}\right\} \Rightarrow w_{iG} = w_G\cos\left(\frac{2\pi}{3}(i-1) + \psi\right), \quad i = 1, 2, 3. \tag{14}$$

Note that w_i represents transverse vibration[25] in body coordinate system $x_i w_i$. By summing the three equations in Eq. (13) and next, the three equations in Eq. (14), we can write

$$x_{1G} + x_{2G} + x_{3G} = 0, \tag{15}$$

$$w_{1G} + w_{2G} + w_{3G} = 0. \tag{16}$$

Equation (16) represents a constraint equation for the transverse vibrations of the three beams at junction point, *G*. Additional constraint equations can be written at junction point, *G*. Note that three

https://doi.org/10.1017/S0263574714001398 Published online by Cambridge University Press

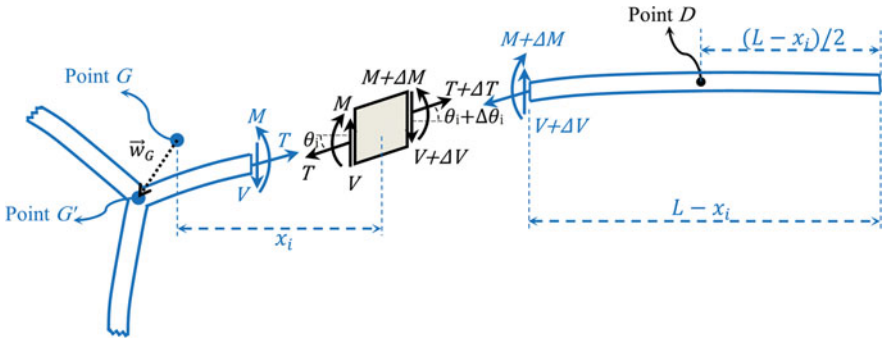


Fig. 5. An arbitrary beam element and its left and right side of the beam element.

beams of the moving platform are assumed to be welded together at point G. Therefore, for both the rigid as well as the flexible moving platform, the angles between the lines starting at point G and tangent to the three beams remain at the constant value of 120°. Therefore, two additional constraint equations can be written as

$$\left(\frac{\partial w_1}{\partial x_1}\right)_G = \left(\frac{\partial w_2}{\partial x_2}\right)_G = \left(\frac{\partial w_3}{\partial x_3}\right)_G. \tag{17}$$

5. Effect of Vibrating Motion of the Moving Platform on the Beams Axial Acceleration

The three beams of the moving platform are assumed to be axially rigid. As stated in Section 3, due to rigid body motion of the robot, the rigid acceleration of each element of the beam in direction x_i is defined as a_{xi} (Eq. (11)). Consider Fig. 2(b). Vibration of the moving platform causes point G to reach to point G'. This elastic displacement causes additional axial motion of each beam which must be added to the rigid axial displacement x_{iG}. Therefore, axial acceleration of each element of the moving platform has an additional component due to the vibrating motion of the moving platform. This introduces few nonlinear terms in the motion equations which will be further discussed in later sections. From the three equations of Eq. (14), expressions $\cos(\psi)$, $\sin(\psi)$, and w_G are obtained in terms of w_{1G}, w_{2G}, and w_{3G} and substituted into Eq. (13). Therefore, x_{1G}, x_{2G}, and x_{3G} in Eq. (13) are obtained in terms of w_{1G}, w_{2G}, and w_{3G} as follows:

$$\begin{aligned} x_{1G} &= (-w_{2G} + w_{3G})/\sqrt{3} \\ x_{2G} &= (-w_{3G} + w_{1G})/\sqrt{3}. \\ x_{3G} &= (-w_{1G} + w_{2G})/\sqrt{3} \end{aligned} \tag{18}$$

By differentiating the above equation, we have

$$\begin{aligned} \ddot{x}_{1G} &= (-\ddot{w}_{2G} + \ddot{w}_{3G})/\sqrt{3} \\ \ddot{x}_{2G} &= (-\ddot{w}_{3G} + \ddot{w}_{1G})/\sqrt{3}, \\ \ddot{x}_{3G} &= (-\ddot{w}_{1G} + \ddot{w}_{2G})/\sqrt{3} \end{aligned} \tag{19}$$

in which $\ddot{x}_{iG}$ is relative axial acceleration due to elastic motion with respect to the $x_i w_i$ body coordinate system. Note that the beams are assumed to be axially rigid. Therefore, for any beam, the values of $\ddot{x}_{iG}$ are equal for all of its elements. This means that in addition to point G, Eq. (19) may also be used to show the relative axial acceleration for any element of each beam.

Consider Fig. 5. To obtain the axial inertia force acting on the beam at an arbitrary position x_i, the part of the beam on the right side of the element is considered. Point D represents the center of mass of the beam on the right side of the element. For the beam element at x_i position, the rigid axial acceleration was shown in Eq. (11). Then, the rigid axial acceleration at direction x_i for point D can

https://doi.org/10.1017/S0263574714001398 Published online by Cambridge University Press

be written as

$$(a_{xi})_D = a_G.\hat{e}_{xi} - \left(\frac{x_i + L}{2}\right)\dot{\theta}^2, \quad \hat{e}_{xi} = \begin{bmatrix} \sin(\theta + (i-1)\,2\pi/3) \\ -\cos(\theta + (i-1)\,2\pi/3) \end{bmatrix}, \quad i = 1, 2, 3. \tag{20}$$

Using the above equation, the total axial acceleration for point D in x_i direction can be obtained by summing axial acceleration due to rigid and elastic motion as

$$\begin{aligned} a'_{xi}(x_i, t) &= (a_{xi})_D + \left(-w_i\left(\frac{x_i + L}{2}, t\right)\ddot{\theta} - x_{iG}\dot{\theta}^2 - 2\dot{w}_i\left(\frac{x_i + L}{2}, t\right)\dot{\theta} + \ddot{x}_{iG}\right) \\ &= \mathbf{a}_G.\hat{\mathbf{e}}_{xi} - \left(\frac{x_i + L}{2}\right)\dot{\theta}^2 + \left(-w_i\left(\frac{x_i + L}{2}, t\right)\ddot{\theta} - x_{iG}\dot{\theta}^2 - 2\dot{w}_i\left(\frac{x_i + L}{2}, t\right)\dot{\theta} + \ddot{x}_{iG}\right), \\ & i = 1, 2, 3, \end{aligned} \tag{21}$$

in which $(-w_i(\frac{x_i+L}{2}, t)\ddot{\theta} - x_{iG}\dot{\theta}^2 - 2\dot{w}_i(\frac{x_i+L}{2}, t)\dot{\theta} + \ddot{x}_{iG})$ is the axial acceleration of point D due to elastic and rotational motions of the $x_i w_i$ body coordinate system. Equation (21) can be used for computing the axial inertia force in each beam. In Fig. 5, parameters T, V, and M represent the inertia axial force, shear force, and bending moment respectively. Parameter θ_i represents the slope angle of deformation of beam i.

6. Motion Equation and Applying the Constraints

Robot dynamics can be viewed as both direct and inverse dynamic problems. In the direct dynamics, motor torques/forces are supplied and resulting robot motion is obtained. Conversely, in the inverse dynamic problem, motion of the robot is supplied and required motor torques/forces are obtained. In this section, dynamic model of the ST robot is obtained which can be used for both the direct and inverse dynamic problems.

Authors of the present paper in ref. [14] have presented a differential equation for planar vibrating motion of an Euler–Bernoulli beam having a prismatic joint. The authors assumed both vibration amplitude and slope angle of deformation to be small in their analytical model. Additionally, similar to the present study, the differential equation was written using a rigid body coordinate system. In the present research, the same motion equation and solution method presented in ref. [14] are used and relevant constraint equations are added to the motion equation using Lagrange's multipliers. Therefore, the motion equation for the ST robot for an element at x_i position can be written as

$$\begin{aligned} &\left[\rho\left(\frac{\partial^2 w_i}{\partial t^2} + x_{iG}\ddot{\theta} - w_i\dot{\theta}^2 + 2\dot{x}_{iG}\dot{\theta}\right) + \frac{\partial^2}{\partial x_i^2}\left(EI\frac{\partial^2 w_i}{\partial x_i^2}\right) + \frac{\partial}{\partial x_i}\left(\rho\,(L - x_i)\,a'_{xi}(x_i, t)\frac{\partial w_i}{\partial x_i}\right)\right]\delta w_i\,(x_i) \\ &\quad = -\rho a_{wi}\,(x_i, t)\,\delta w_i\,(x_i) + F_{pi}\mathrm{dirac}(x_i - x_{pi})\delta w_i(x_{pi}), \quad i = 1, 2, 3, \end{aligned} \tag{22}$$

in which $(\partial^2 w_i/\partial t^2 + x_{iG}\ddot{\theta} - w_i\dot{\theta}^2 + 2\dot{x}_{iG}\dot{\theta})$ is the vertical acceleration of the element due to elastic and rotational motion of the $x_i w_i$ body coordinate system. Parameters x_{pi}, $a_{wi}(x_i, t)$, and $a'_{xi}(x_i, t)$ are determined by Eqs. (10), (12), and (21) respectively. Parameters ρ, EI, and L are mass per length, bending rigidity, and beam length, respectively, and are equal for all the three beams. Parameter F_{pi} is the normal force that is applied on beam i at $x_i = x_{pi}$ by the prismatic joint. It is assumed that all friction forces are negligible. The term $\frac{\partial}{\partial x_i}(\rho(L - x_i)a'_{xi}(x_i, t)\frac{\partial w_i}{\partial x_i})$ used in Eq. (22) represents the variation of the axial inertia force in vibration direction, vertical direction, of beam

$$\begin{aligned} &\frac{\partial}{\partial x_i}\left(\rho\,(L - x_i)\,a'_{xi}(x_i, t)\frac{\partial w_i}{\partial x_i}\right) \\ &\quad = -\rho a'_{xi}\,(x_i, t)\,\frac{\partial w_i}{\partial x_i} + \rho\,(L - x_i)\,\frac{\partial a'_{xi}(x_i, t)}{\partial x_i}\frac{\partial w_i}{\partial x_i} + \rho\,(L - x_i)\,a'_{xi}(x_i, t)\frac{\partial^2 w_i}{\partial x_i^2} \approx 0. \end{aligned} \tag{23}$$

https://doi.org/10.1017/S0263574714001398 Published online by Cambridge University Press

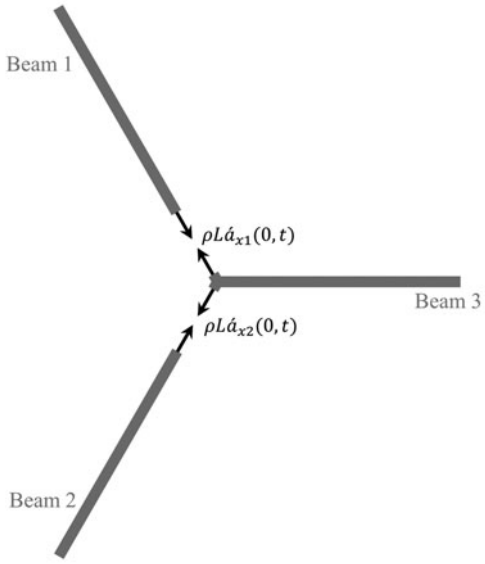


Fig. 6. The axial inertia force of two beams and their reaction forces acting on the third beam.

The value of the above nonlinear expression is small due to the assumption of small slope angle for the beams' deformation.[14] Therefore, comparing with other terms of Eq. (22), the expression shown in Eq. (23) may be neglected. However, it should be noted that although the inertia force of each beam acting on point G, $\rho(L-0)a'_{xi}(0,t)$, is insignificant, its effect on the transverse vibration of the other two beams is significant. See Fig. 6. This effect must be considered using a suitable method.

To consider the effect of the inertia force on the transverse vibration of the other two beams, constraint Eqs. (18) is written in the form of virtual displacement as

$$\begin{aligned} &F_{1x}(\delta x_{1G} + \delta w_{2G}/\sqrt{3} - \delta w_{3G}/\sqrt{3}) = 0 \\ &F_{2x}(\delta x_{2G} + \delta w_{3G}/\sqrt{3} - \delta w_{1G}/\sqrt{3}) = 0 \\ &F_{3x}(\delta x_{3G} + \delta w_{1G}/\sqrt{3} - \delta w_{2G}/\sqrt{3}) = 0, \end{aligned} \tag{24}$$

in which parameters F_{ix} are proper Lagrange's multipliers that represent the axial inertia forces at the center of the star. Also from Eq. (17), we have

$$\begin{aligned} &M_{1G}\left(\delta\left(\frac{\partial w_1}{\partial x_1}\right)_G - \delta\left(\frac{\partial w_2}{\partial x_2}\right)_G\right) = 0, \\ &M_{3G}\left(\delta\left(\frac{\partial w_3}{\partial x_3}\right)_G - \delta\left(\frac{\partial w_2}{\partial x_2}\right)_G\right) = 0, \end{aligned} \tag{25}$$

in which parameters M_{1G} and M_{3G} are proper Lagrange's multipliers that represent the bending moments at the center of the star, point G, in beams 1 and 3 respectively. As can be seen from Eq. (25), virtual work of M_{1G} and M_{3G} are $M_{1G}\delta(\partial w_1/\partial x_1)_G$ and $M_{3G}\delta(\partial w_3/\partial x_3)_G$ for virtual displacements of $\delta(\partial w_1/\partial x_1)_G$ and $\delta(\partial w_3/\partial x_3)_G$ respectively. In addition, their virtual work is $(-M_{1G} - M_{3G})\delta(\partial w_2/\partial x_2)_G$ in which coefficient of virtual displacement of $\delta(\partial w_2/\partial x_2)_G$ represents the value of M_{2G}. Therefore, $M_{2G} = -M_{1G} - M_{3G}$. This shows the equilibrium of bending moments at point G:

$$M_{1G} + M_{2G} + M_{3G} = 0. \tag{25–1}$$

Also, from Eq. (16) we have

$$F_w\,(\delta w_{1G} + \delta w_{2G} + \delta w_{3G}) = 0, \tag{26}$$

https://doi.org/10.1017/S0263574714001398 Published online by Cambridge University Press

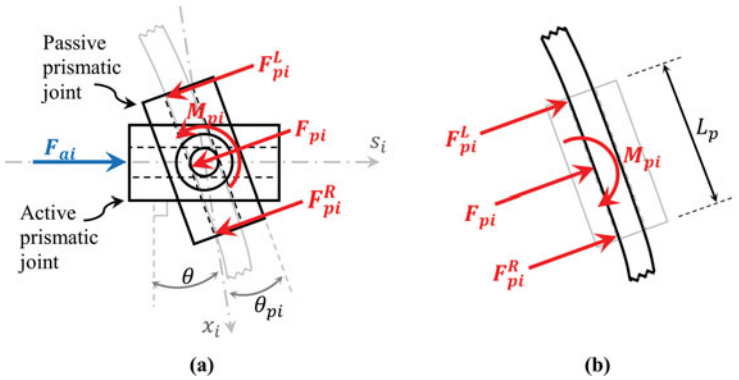


Fig. 7. (a) Free body diagram of rigid parts of each robot leg; (b) Prismatic joint effects on the beam.

in which F_w is a proper Lagrange's multiplier that represents a shear force at the center of the star. Additional constraints can be written for displacement of the positions on the moving platform where the prismatic joints are located, as

$$F_{pi}\delta w_i(x_{pi}) = 0, \quad i = 1, 2, 3. \tag{27}$$

The above constraint equation is already applied in Eq. (22). As stated earlier, F_{pi} is the normal contact force that the prismatic joint applies to the beam at $x_i = x_{pi}$. Amount of the slope angle of deformation at points x_{pi} is called θ_{pi}. To apply the effect of prismatic joint length L_p following constraints can be written using Lagrange's multipliers F_{pi}^R and F_{pi}^L as

$$\begin{aligned} F_{pi}^R\left(\delta w_i\left(x_{pi} + L_p/2\right) - \tfrac{L_p}{2}\delta\theta_{pi}\right) = 0, \quad i = 1, 2, 3, \\ F_{pi}^L\left(\delta w_i\left(x_{pi} - L_p/2\right) + \tfrac{L_p}{2}\delta\theta_{pi}\right) = 0, \quad i = 1, 2, 3, \end{aligned} \tag{28}$$

in which the Lagrange's multipliers F_{pi}^R and F_{pi}^L represent normal surface forces that are applied to the beam by the prismatic joint at its right and left edges, respectively (Fig. 7(b)).

Next, the effect of rotational inertia of the prismatic joints in the dynamic model is considered as

$$\theta_{pi} = \left.\frac{\partial w_i(x_i, t)}{\partial x_i}\right|_{x_i = x_{pi}} = \frac{\partial w_i}{\partial x_i}(x_{pi}, t) \Rightarrow \quad M_{pi}\left(\delta\theta_{pi} - \delta\frac{\partial w_i}{\partial x_i}(x_{pi})\right) = 0, \quad i = 1, 2, 3, \tag{29}$$

in which M_{pi} is a Lagrange's multiplier and represents the moment that the beam applies on the corresponding prismatic joint.

According to constraint Eq. (24), the axial displacements of beams x_{iG} are included in the dynamic model. Then, to solve for x_{iG}, motion equations for axial motion of the beams are obtained by considering the virtual work principle, Eqs. (21) and (24) as

$$\begin{aligned} &(\rho L)\, a'_{xi}\,(0, t)\,\delta x_{iG} = F_{ix}\delta x_{iG}, \quad i = 1, 2, 3, \\ &\Rightarrow \rho L\left(a_G.\hat{e}_{xi} - \left(\frac{L}{2}\right)\dot{\theta}^2 + \left(-w_i\left(\frac{L}{2}, t\right)\ddot{\theta} - x_{iG}\dot{\theta}^2 - 2\dot{w}_i\left(\frac{L}{2}, t\right)\dot{\theta} + \ddot{x}_{iG}\right)\right) = F_{ix}. \end{aligned} \tag{30}$$

Similarly, according to constraint Eq. (29), the angular positions of prismatic joints θ_{pi} are included in the dynamic model. Then, to solve for θ_{pi}, motion differential equations for angular motion of the

https://doi.org/10.1017/S0263574714001398 Published online by Cambridge University Press

prismatic joints are obtained by considering the virtual work principle (Eqs. (28) and (29)) as

$$J_p \frac{\mathrm{d}^2}{\mathrm{d}t^2}(\theta + \theta_{pi})\delta\theta_{pi} = M_{pi}\delta\theta_{pi} + \left(F_{pi}^L - F_{pi}^R\right)\frac{L_p}{2}\delta\theta_{pi}$$
$$\Rightarrow J_p \frac{\mathrm{d}^2}{\mathrm{d}t^2}(\theta + \theta_{pi}) = M_{pi} + \left(F_{pi}^L - F_{pi}^R\right)\frac{L_p}{2}, \quad i = 1, 2, 3, \tag{31}$$

in which J_p is rotational moment of each passive prismatic joint. This differential equation, Eq. (31), is a motion equation for the rotational motion of the prismatic joints. By simultaneously solving Eq. (31) with other motion and constraint equations, the effect of rotational inertia moment of the prismatic joints on the vibration of the moving platform is considered in the dynamic model. Neglecting the small terms (Eq. (23)), and applying the constraint equations by the Lagrange's multipliers method (Eqs. (24)–(29)), the vibrational motion equation for each beam of the moving platform (Eq. (22)) can be written as

$$\begin{aligned}
&\left[\rho\left(\frac{\partial^2 w_i}{\partial t^2} + x_{iG}\ddot{\theta} - w_i\dot{\theta}^2 + 2\dot{x}_{iG}\dot{\theta}\right) + \frac{\partial^2}{\partial x_i^2}\left(EI\frac{\partial^2 w_i}{\partial x_i^2}\right)\right]\delta w_i\,(x_i) \\
&= -\rho a_{wi}(x_i, t)\delta w_i(x_i) + F_{pi}\mathrm{dirac}(x_i - x_{pi})\delta w_i(x_{pi}) \\
&\quad + F_{pi}^L\mathrm{dirac}\left(x_i - x_{pi} + \frac{L_p}{2}\right)\delta w_i\left(x_{pi} - \frac{L_p}{2}\right) \\
&\quad + F_{pi}^R dirac\left(x_i - x_{pi} - \frac{L_p}{2}\right)\delta w_i\left(x_{pi} + \frac{L_p}{2}\right) \\
&\quad - M_{pi}\mathrm{dirac}(x_i - x_{pi})\delta\frac{\partial w_i}{\partial x_i}(x_{pi}) \\
&\quad + \frac{1}{\sqrt{3}}\left(F_{i+2,x} - F_{i+1,x}\right)\mathrm{dirac}\,(x_i - 0)\,\delta w_i\,(0) \\
&\quad + M_{iG}\mathrm{dirac}\,(x_i - 0)\,\delta\frac{\partial w_i}{\partial x_i}\,(0) + F_w\mathrm{dirac}\,(x_i - 0)\,\delta w_i\,(0)\,, \quad i = 1, 2, 3, \\
&\quad \times \text{and, ifindex}\,\{i + (1\,\text{or}\,2)\} > 3\ \text{then}\ \{i + 1\,\text{or}\,2\} = \{i + (1\,\text{or}\,2) - 3\}\,.
\end{aligned} \tag{32}$$

To obtain the vibration response of the ST robot, the motion equations, Eqs. (30)–(32), must be simultaneously solved with the constraint equations, Eqs. (24)–(29). Upon solving these equations, parameters F_{pi} and θ_{pi} are determined. In addition, by specifying mass of the prismatic joints, required driving forces, F_{ai}, can be determined as follows:

$$(m_{pp} + m_{pa})s_i\,(t) = F_{ai} - \left(F_{pi} + F_{pi}^L + F_{pi}^R\right)\cos\left(\theta + \theta_{pi}\right), \quad i = 1, 2, 3, \tag{33}$$

in which parameters m_{pp} and m_{pa} represent masses for the passive and the active prismatic joints, respectively. Note that the two prismatic joints are joined by a revolute joint (see Fig. 7(a)). Upon obtaining F_{ai}, the inverse dynamics problem of the ST robot is solved. It should be noted that the same formulation allows solving for the direct dynamics problem of the robot. This may be accomplished by specifying the driving forces, F_{ai}, in Eq. (33) and solving a new set of motion equations, Eqs. (30)–(33) simultaneously, with the constraint Eqs. (24)–(29).

7. Solution of the Motion Equations

In this section, the "constrained assumed modes method" is further developed to solve the derived motion equations of the ST parallel robot. Consider the ST robot in its rigid case. This robot has three modes of operation, pure rotation, pure translation, and mixed type, which includes both rotation and translation of the moving platform. In pure rotational mode, the center of the star, point G, remains fixed and the star does a rotational motion about G. In translational mode, the angular position is

https://doi.org/10.1017/S0263574714001398 Published online by Cambridge University Press

fixed, and the star does a translational motion. In the flexible case, the same modes of operation are also investigated. The four different motion types induce different acceleration and inertia forces and consequently different boundary conditions at point G. Therefore, in order to solve the motion equations, different mode shapes of Euler–Bernoulli beam are used for each of the four different motion types. Transverse vibration of the beams of the star can be written as a combination of mode shapes of the Euler–Bernoulli beam as follows:

$$w_i\left(x_i, t\right) = \sum_{m=1}^{N} \alpha_{im}\left(t\right) \varphi_m(x_i), \quad i = 1, 2, 3\,, \tag{34}$$

in which

$$\begin{aligned} \varphi_m\left(x\right) &= A_m \sin\left(\beta_m x\right) + B_m \cos\left(\beta_m x\right) + C_m \sin h\left(\beta_m x\right) + D_m \cos h\left(\beta_m x\right) \\ &\Rightarrow \begin{cases} \left(\frac{EI}{\rho}\right) \frac{\partial^4 \varphi_m}{\partial x^4} = \lambda_m \varphi_m \\ \lambda_m = \omega_m^2 = \frac{EI}{\rho} \beta_m^4 \end{cases}. \end{aligned} \tag{34–1}$$

Therefore, variations of transverse vibration can be written as

$$\delta w_i\left(x_i, t\right) = \sum_{m=1}^{N} \varphi_m(x_i) \delta\alpha_{im}\left(t\right), \quad i = 1, 2, 3. \tag{35}$$

Substituting Eqs. (34) and (35) in motion Eq. (32), we have

$$\begin{aligned} &\left[\sum_{m=1}^{N} \varphi_m(x_i)\ddot{\alpha}_{im}(t) + (x_{iG}\ddot{\theta} + 2\dot{x}_{iG}\dot{\theta}) + (\lambda_m - \dot{\theta}^2) \sum_{m=1}^{N} \varphi_m(x_i)\alpha_{im}(t)\right] \sum_{j=1}^{N} \varphi_j(x_i)\delta\alpha_{ij}(t) \triangleright \\ &= -a_{wi}(x_i, t) \sum_{j=1}^{N} \varphi_j(x_i)\delta\alpha_{ij}(t) + \frac{F_{pi}}{\rho} \text{dirac}(x_i - x_{pi}) \sum_{j=1}^{N} \varphi_j(x_{pi})\delta\alpha_{ij}(t) \\ &\quad + \frac{F_{pi}^L}{\rho} \text{dirac}\left(x_i - x_{pi} + \frac{L_p}{2}\right) \sum_{j=1}^{N} \left(\varphi_j\left(x_{pi} + \frac{L_p}{2}\right) - \varphi_j(x_i)\right) d\alpha_{ij}(t) \\ &\quad + \frac{F_{pi}^R}{\rho} \text{dirac}\left(x_i - x_{pi} + \frac{L_p}{2}\right) \sum_{j=1}^{N} \left(\varphi_j\left(x_{pi} + \frac{L_p}{2}\right) - \varphi_j(x_i)\right) d\alpha_{ij}(t) \\ &\quad - \frac{M_{pi}}{\rho} \text{dirac}(x_i - x_{pi}) \sum_{j=1}^{N} \dot{\varphi}_j(x_{pi})\delta\alpha_{ij}(t) \\ &\quad + \frac{(F_{i+2x} - F_{i+1x})}{\rho\sqrt{3}} \text{dirac}(x_i - 0) \sum_{j=1}^{N} \varphi_j(0)\delta\alpha_{ij}(t) \\ &\quad + \frac{M_{iG}}{\rho} \text{dirac}(x_i - 0) \sum_{j=1}^{N} \dot{\varphi}_j(0)\delta\alpha_{ij}(t) + \frac{F_w}{\rho} \text{dirac}(x_i - 0) \sum_{j=1}^{N} \varphi_j(0)\delta\alpha_{ij}(t), \quad i = 1, 2, 3, \\ &\times \text{and, ifindex } \{i + (1 \text{ or } 2)\} > 3 \text{ then } \{i + 1 \text{ or } 2\} = \{i + (1 \text{ or } 2) - 3\}\,. \end{aligned} \tag{36}$$

https://doi.org/10.1017/S0263574714001398 Published online by Cambridge University Press

By integrating the above equation along the length of the beams, using orthogonality of mode shapes and separating the equation due to coefficients $\delta\alpha_{ij}(t)$, the following equations are obtained:

$$\begin{aligned}
&\ddot{\alpha}_{ij}(t) + \left(\lambda_j - \dot{\theta}^2\right)\alpha_{ij}(t) + \left(x_{iG}\ddot{\theta} + 2\dot{x}_{iG}\dot{\theta}\right)\left(\int_0^L \varphi_j(x_i)\,dx_i\right) \\
&= -\sum_{m=1}^{N}\int_0^L \left(a_{wi}(x_i,t)\varphi_j(x_i)dx_i\right) + \frac{F_{pi}}{\rho}\varphi_j(x_{pi}) \\
&\quad + \frac{F_{pi}^L}{\rho}\left(\varphi_j(x_{pi} - \frac{L_p}{2}) - \varphi_j(x_i)\right) + \frac{F_{pi}^R}{\rho}\left(\varphi_j(x_{pi} + \frac{L_p}{2}) - \varphi_j(x_i)\right) \\
&\quad - \frac{M_{pi}}{\rho}\varphi_j'(x_{pi}) + \frac{(F_{i+2,x} - F_{i+1,x})}{\rho\sqrt{3}}\varphi_j(0) + \frac{M_{iG}}{\rho}\varphi_j'(0) + \frac{F_w}{\rho}\varphi_j(0), \\
&\quad \times j = 1,\ldots,N \quad \text{and} \quad i = 1,2,3, \\
&\quad \times \text{if} \;\; \{i + (1 \text{ or } 2)\} > 3 \text{ then } \{i + 1 \text{ or } 2\} = \{i + (1 \text{ or } 2) - 3\}.
\end{aligned} \tag{37}$$

Note that Eq. (37) includes $3N$ number of independent motion equations. In addition, using Eqs. (34) and (35), the constraint Eqs. (24)–(29) can be written as

$$\begin{cases}
x_{1G} - \sum_{j=1}^{N}\alpha_{2j}(t)\,\varphi_j(0)/\sqrt{3} + \sum_{j=1}^{N}\alpha_{3j}(t)\,\varphi_j(0)/\sqrt{3} = 0 \\
x_{2G} - \sum_{j=1}^{N}\alpha_{3j}(t)\,\varphi_j(0)/\sqrt{3} + \sum_{j=1}^{N}\alpha_{1j}(t)\,\varphi_j(0)/\sqrt{3} = 0 \\
x_{3G} - \sum_{j=1}^{N}\alpha_{1j}(t)\,\varphi_j(0)/\sqrt{3} + \sum_{j=1}^{N}\alpha_{2j}(t)\,\varphi_j(0)/\sqrt{3} = 0
\end{cases}, \tag{38}$$

$$\begin{cases}
\sum_{j=1}^{N}\varphi_j'(0)\left(\alpha_{1j}(t) - \alpha_{2j}(t)\right) = 0 \\
\sum_{j=1}^{N}\varphi_j'(0)\left(\alpha_{3j}(t) - \alpha_{2j}(t)\right) = 0
\end{cases}, \tag{39}$$

$$M_{1G} + M_{2G} + M_{3G} = 0, \tag{39–1}$$

$$\sum_{j=1}^{N}\varphi_j(0)\left(\alpha_{1j}(t) + \alpha_{2j}(t) + \alpha_{3j}(t)\right) = 0, \tag{40}$$

$$\sum_{j=1}^{N}\varphi_j(x_{pi})\alpha_{ij}(t) = 0, \quad i = 1,2,3, \tag{41}$$

$$\begin{cases}
-\frac{L_p}{2}\delta\theta_{pi} + \sum_{j=1}^{N}\varphi_j\left(x_{pi} + \frac{L_p}{2}\right)\alpha_{ij}(t) - \varphi_j(x_{pi})\alpha_{ij}(t) = 0 \\
+\frac{L_p}{2}\delta\theta_{pi} + \sum_{j=1}^{N}\varphi_j\left(x_{pi} - \frac{L_p}{2}\right)\alpha_{ij}(t) - \varphi_j(x_{pi})\alpha_{ij}(t) = 0
\end{cases}, \quad i = 1,2,3, \tag{42}$$

https://doi.org/10.1017/S0263574714001398 Published online by Cambridge University Press

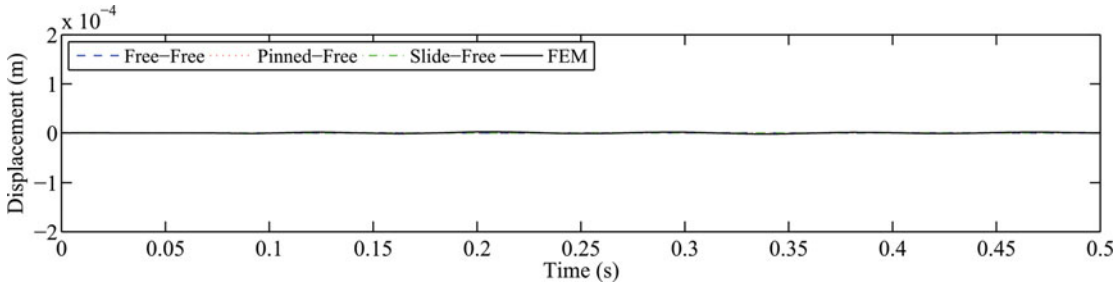


Fig. 8. Case study 1: elastic displacement of point G measured in the rigid body coordinate system $x_1 w_1$.

$$\theta_{pi} - \sum_{j=1}^{N} \varphi_j'(x_{pi})\alpha_{ij}(t) = 0, \quad i = 1, 2, 3. \tag{43}$$

Substituting Eq. (34) into Eq. (30), we have

$$\mathbf{a}_G.\hat{\mathbf{e}}_{xi} - \left(\frac{L}{2}\right)\dot{\theta}^2 + \left(\ddot{x}_{iG} - x_{iG}\dot{\theta}^2 - \ddot{\theta}\sum_{m=1}^{N}\varphi_m\left(\frac{L}{2}\right)\alpha_{im}(t) - 2\dot{\theta}\sum_{m=1}^{N}\varphi_m\left(\frac{L}{2}\right)\alpha_{im}(t)\right)$$
$$= F_{ix}/(\rho L), \quad i = 1, 2, 3. \tag{44}$$

To obtain the unknown parameters $\alpha_{im}(t)$, $x_{iG}(t)$, and $\theta_{pi}(t)$, motion Eqs. (31), (37), and (44) must be solved along with constraint Eqs. (38)–(43). In addition, the solution provides the constraint forces/moments or the Lagrange's multipliers.

8. Numerical Results

In this section, four case studies, each with a different type of motion, are considered as follows:

Case study 1: In place rotation	$s_1(t) = s_2(t) = s_3(t) = t^2$
Case study 2: Rectilinear translation	$s_1(t) = t^2,\ s_2(t) = -0.5t^2,\ s_3(t) = -0.5t^2$
Case study 3: General plane motion	$s_1(t) = t^2,\ s_2(t) = 0,\ s_3(t) = 0.5t^2$
Case study 4: A specific rectilinear translation	$s_1(t) = t^2,\ s_2(t) = -t^2,\ s_3(t) = 0$

In all four cases, it is assumed that the robot starts in the configuration shown in Fig. 2(a). For each of the four case studies, three different groups of mode shapes are used to solve the analytical motion equations. For point G, three different boundary conditions, pinned, slide, and free, are assumed while for the free ends of the beams, points A, B, and C, we use only the free boundary conditions. Therefore, the first group uses pinned-free mode shapes, second uses slide-free mode shapes, and third uses free-free mode shapes. The results of the analytical method are also compared with FEM results. For each case study, the number of the mode shapes used in the analytical solution is 25 and the number of the elements in FEM solution is 300. A two-node linear beam element is used in the FEM solution. Physical properties of the robot are as $E = 200 \times 10^9 (\mathrm{N/m^2})$, $I = 2.5 \times 10^{-12} (\mathrm{m^4})$, $\rho = 0.234\,(\mathrm{kg/m})$, $d = 0.18\,(\mathrm{m})$, $L = 0.5\,(\mathrm{m})$, $L_p = 0.03\,(\mathrm{m})$, $m_{pp} + m_{pa} = 0.2\,(\mathrm{kg})$, and $J_p = 2 \times 10^{-4}\ (\mathrm{kg\,m^2})$. Note that the different motions used for the four case studies cause the end-effector to reach its end of travel at different times. Therefore, the simulation time used for the four case studies varies between 0.4 and 0.5 s.

8.1. Case study 1

For case study 1, the robot configuration and the induced motion are symmetric. Therefore, as expected, the center point of the robot remains fixed and does not vibrate. See Fig. 8.

https://doi.org/10.1017/S0263574714001398 Published online by Cambridge University Press

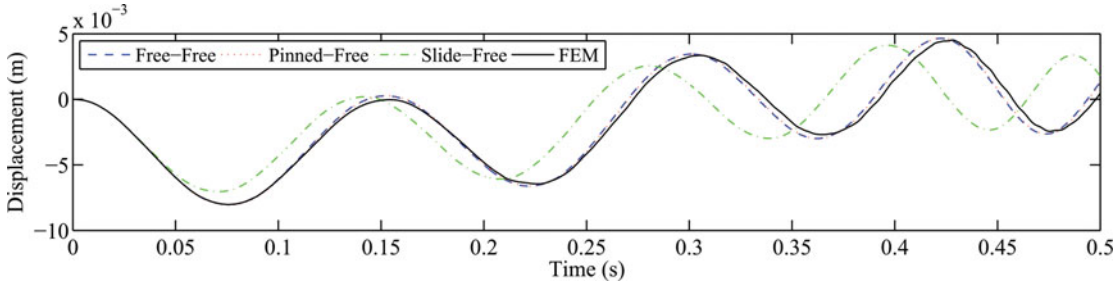


Fig. 9. Case study 1: elastic tip displacement for three beams measured in the rigid body coordinate system $x_1 w_1$.

Next, vibration of the free ends of the beams, points A, B, and C, for case study 1 are considered. Figure 9 demonstrates the elastic tip displacement for point A. The vibration of points B and C for the other two beams are identical to that of point A and therefore are not separately shown.

As shown in Fig. 9, for case study 1, more accurate responses are obtained using the pinned-free and free-free mode shapes than slide-free mode shapes. One important reason for this is that the slide-free mode shapes impose boundary conditions of zero first derivative and non-zero second derivative at the center of the star. However, in case study 1, the symmetric rotational motion causes center of the star to remain in a fixed position, fixed pin, and consequently use of slide-free boundary conditions is not correct. As expected, for case study 1, the most accurate response with respect to FEM solution is obtained using the pinned-free mode shapes. The deformed shape of the moving platform obtained at $t = 0.5$ s using the pinned-free mode shapes, is shown in Fig. 10 for case study 1. As expected, due to symmetrical motion about point G, the deformation of beams 1, 2, and 3 are identical. Amount of the three driving forces, F_{ai}, obtained using pinned-free mode shapes for case study 1 is shown in Fig. 11. Results are compared with the FEM results. Due to the symmetrical motion, the value of all three driving forces is equal.

8.2. Case study 2

The rectilinear trajectory used for case study 2 results in a translational motion in the X direction for the moving star. Elastic displacement of the point G measured in the rigid body coordinate systems is shown in Fig. 12.

The rigid motion trajectory for case study 2 results in point G to vibrate. As intuitively expected and supported by the free-free, slide-free mode shapes and the FEM results shown in Fig. 12, point G vibrates. However, point G does not vibrate when pinned-free mode shapes are used. Therefore, we can safely conclude that result of the pinned-free mode shape as shown in Fig. 12 is not correct. For case study 2, considering the overall behavior, the most accurate response with respect to FEM solution is obtained when the slide-free mode shapes are used. Next, elastic tip displacements for free ends of the three beams, points A, B, and C, are calculated and shown in Fig. 13.

As shown in Fig. 13, similar to the results shown in Fig. 12, the assumption of the pinned-free boundary condition is not correct and considering the overall behavior, the most accurate response with respect to FEM solution is obtained when the slide-free mode shapes are used. The deformed shape of the moving platform obtained at $t = 0.4$ s using the free-free mode shapes, is shown in Fig. 14. Note that the slope of all beams at point G is near zero while second derivative is non-zero. Therefore, the free-free mode shapes cannot satisfy this boundary condition at point G resulting in a less accurate solution. Amount of the driving forces, F_{ai}, obtained using the slide-free mode shapes are shown in Fig. 15. As can be seen from this figure, the results of the analytical solution closely follow the FEM solution.

8.3. Case study 3

Next, elastic displacement of point G for case study 3 is calculated. The elastic displacements measured in the three rigid body coordinate systems are shown in Fig. 16.

Similar to the two previous case studies, elastic tip displacements for three beams are also calculated and shown in Fig. 17. As can be seen from Figs. 16 and 17, for case study 3, the most accurate response with respect to FEM solution is obtained using the free-free mode shapes. The deformed shape of the

https://doi.org/10.1017/S0263574714001398 Published online by Cambridge University Press

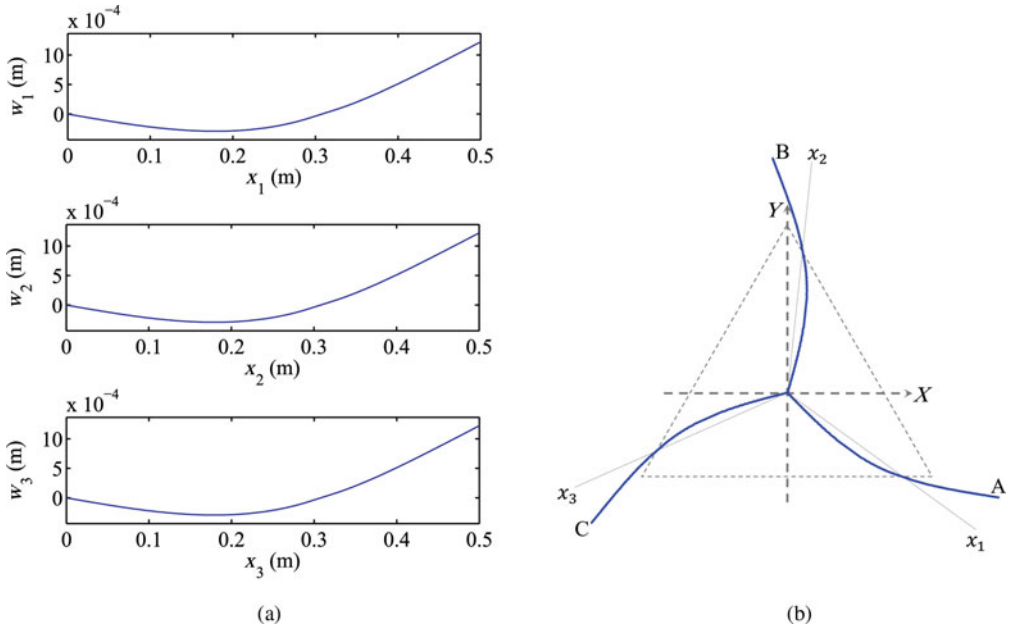


Fig. 10. Case study 1: beam shapes at $t = 0.5$ s; deformation axis is magnified: (a) elastic deformation of beams; (b) approximate rigid and elastic displacement of the star.

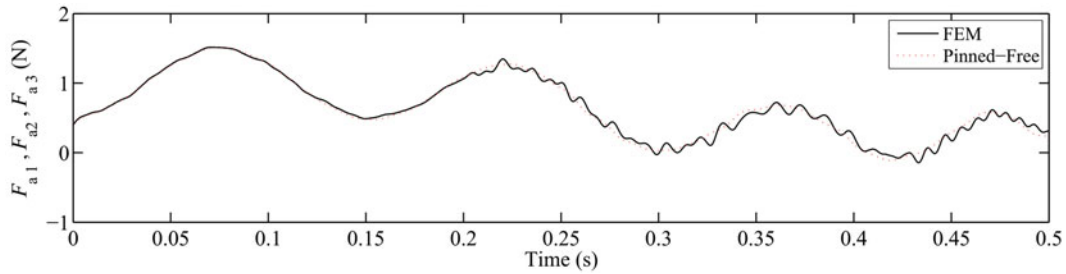


Fig. 11. Case study 1: amount of the three driving forces using pinned-free mode shapes.

moving platform obtained at $t = 0.5$ s using the free-free mode shapes, is shown in Fig. 18 for case study 3.

Note that the slope of all beams at point G is non-zero. This is one of the reasons why the slide-free mode shapes cannot satisfy this boundary condition at point G. Amount of the driving forces, F_{ai}, obtained using the free-free mode shapes are calculated and shown in Fig. 19.

As can be seen from Fig. 19, the results of the analytical solution closely follow the FEM solution.

8.4. Case study 4

The rectilinear translational trajectory used in case study 4, causes beam 3 to only have an axial motion and consequently does not have any transverse vibration. Elastic displacement of the point G measured in the rigid body coordinate systems is shown in Fig. 20.

The rigid motion trajectory for case study 4 results in point G to vibrate. As intuitively expected and supported by the free-free, slide-free mode shapes, and the FEM results shown in Fig. 20, point G vibrates in the x_3 direction. However, as intuitively expected and shown in Fig. 20, point G does not vibrate when pinned-free mode shapes are used. Therefore, we can conclude that result of the pinned-free mode shapes as shown in Fig. 20 is not correct. Additionally, the free-free mode shapes impose boundary conditions of non-zero first derivative and zero second derivative at the center of the star. However, in case study 4, the specific translational motion causes slope of all three beams at point G, $\partial w_i/\partial x_i(0)$, to be zero while the second derivative for beams 1 and 2 at point G are non-zero. The slide-free mode shapes satisfy these boundary conditions at the center of the star. Therefore, for case study 4, the most accurate response with respect to FEM solution is obtained when the slide-free

https://doi.org/10.1017/S0263574714001398 Published online by Cambridge University Press

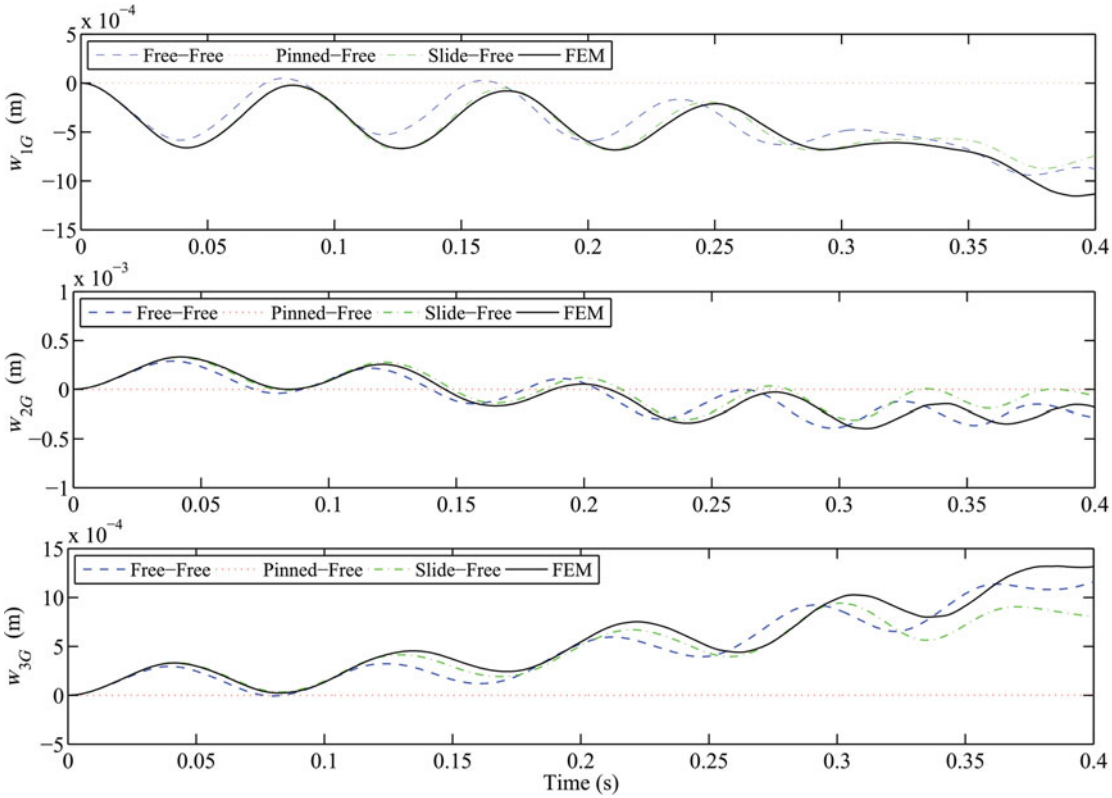


Fig. 12. Case study 2: elastic displacement of point G measured in the rigid body coordinate systems x_1w_1, x_2w_2, and x_3w_3.

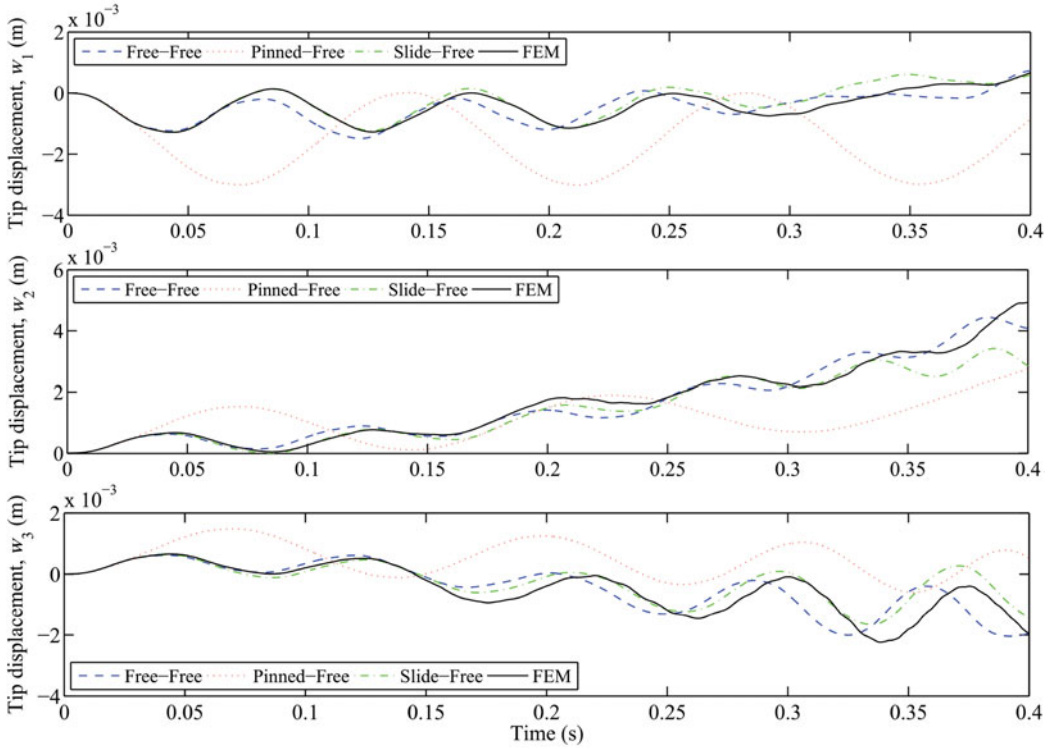


Fig. 13. Case study 2: elastic tip displacements for three beams measured in the rigid body coordinate systems x_1w_1, x_2w_2, and x_3w_3.

https://doi.org/10.1017/S0263574714001398 Published online by Cambridge University Press

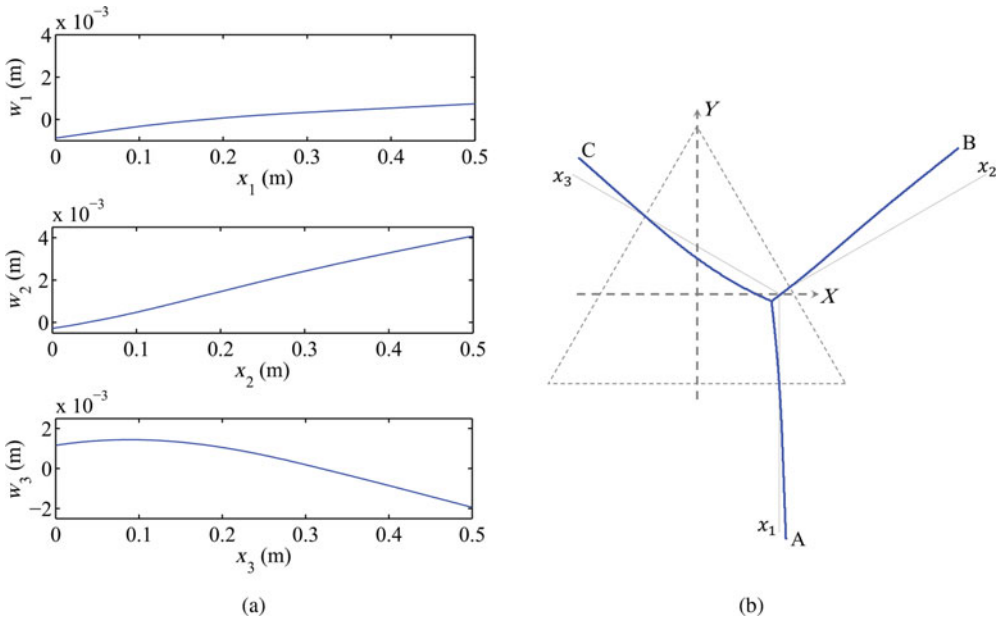


Fig. 14. Case study 2: beam shapes at $t = 0.4$ s; deformation axis is magnified: (a) elastic deformation of beams; (b) approximate rigid and elastic displacement of the star.

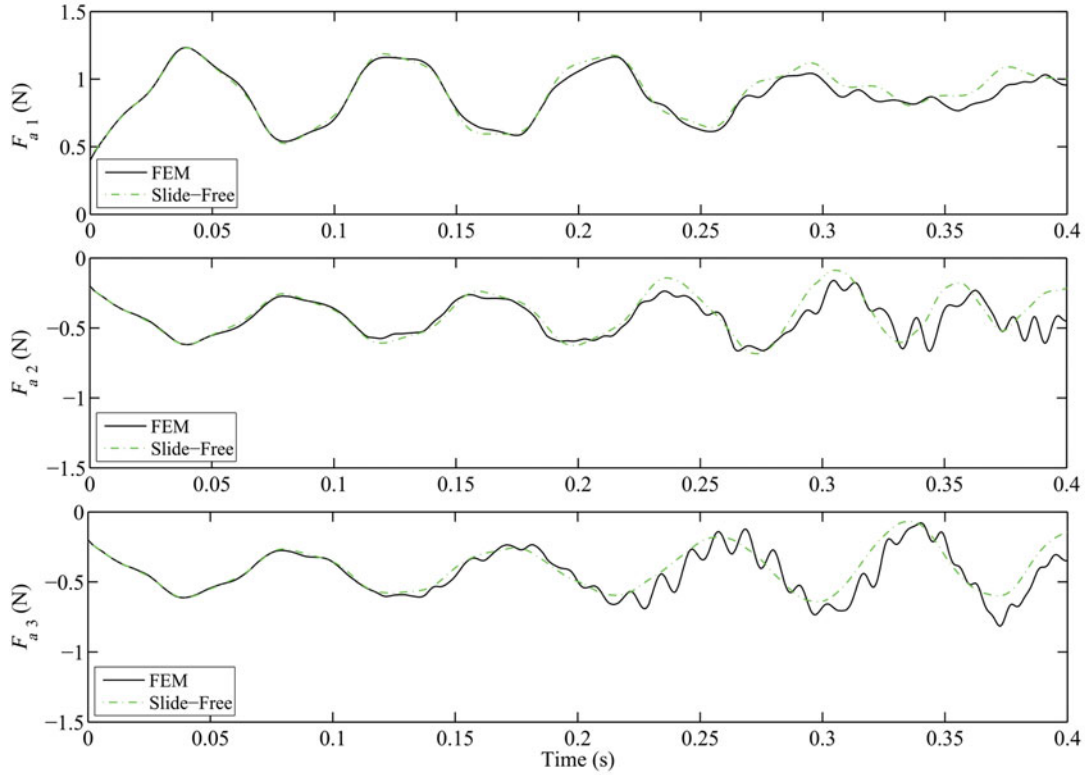


Fig. 15. Case study 2: amount of the three driving forces using slide-free mode shapes.

mode shapes are used. Next, elastic tip displacements for three beams of the moving platform are calculated and shown in Fig. 21.

As shown in Fig. 21, similar to the results shown in Fig. 20, the assumption of pinned-free boundary condition is not correct and the most accurate response with respect to FEM solution is obtained when the slide-free mode shapes are used.

https://doi.org/10.1017/S0263574714001398 Published online by Cambridge University Press

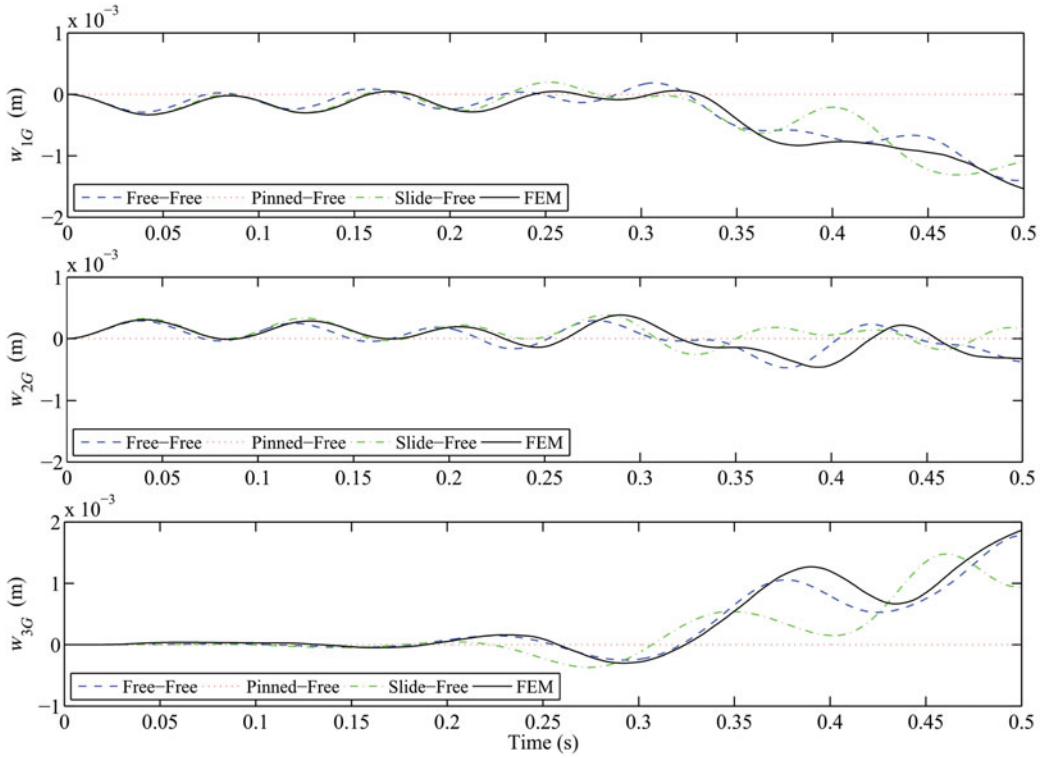


Fig. 16. Case study 3: elastic displacement of point G measured in the rigid body coordinate systems x_1w_1, x_2w_2, and x_3w_3.

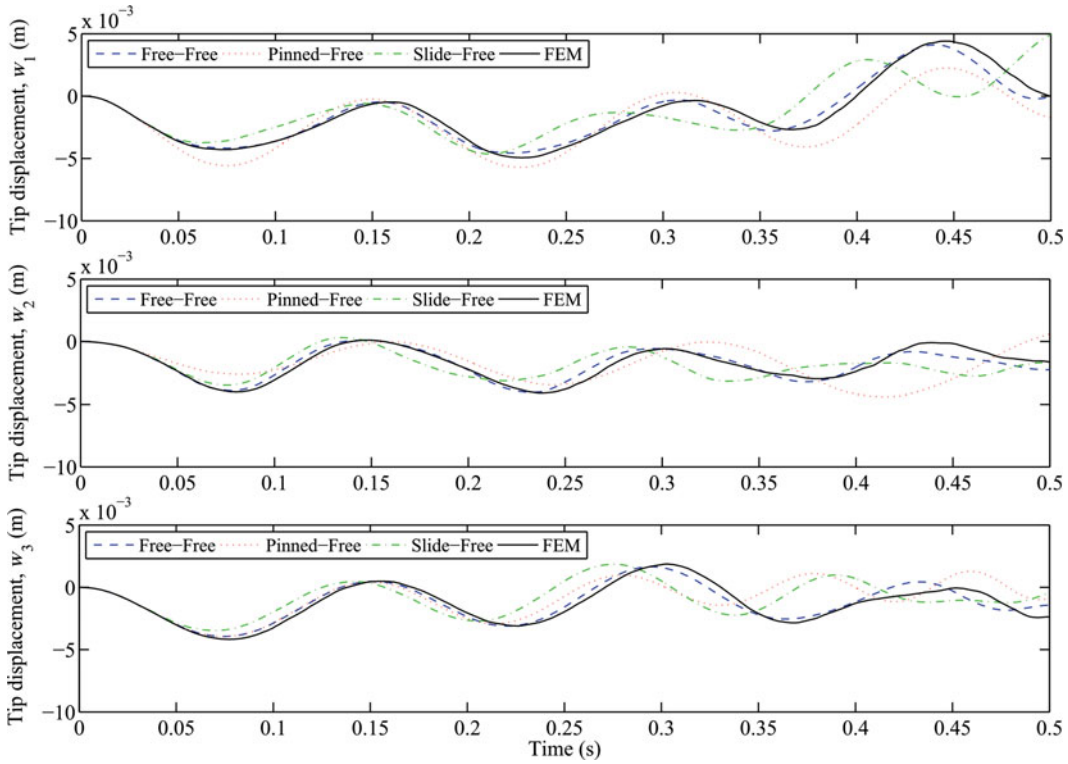


Fig. 17. Case study 3: elastic tip displacements for three beams measured in the rigid body coordinate systems x_1w_1, x_2w_2, and x_3w_3.

https://doi.org/10.1017/S0263574714001398 Published online by Cambridge University Press

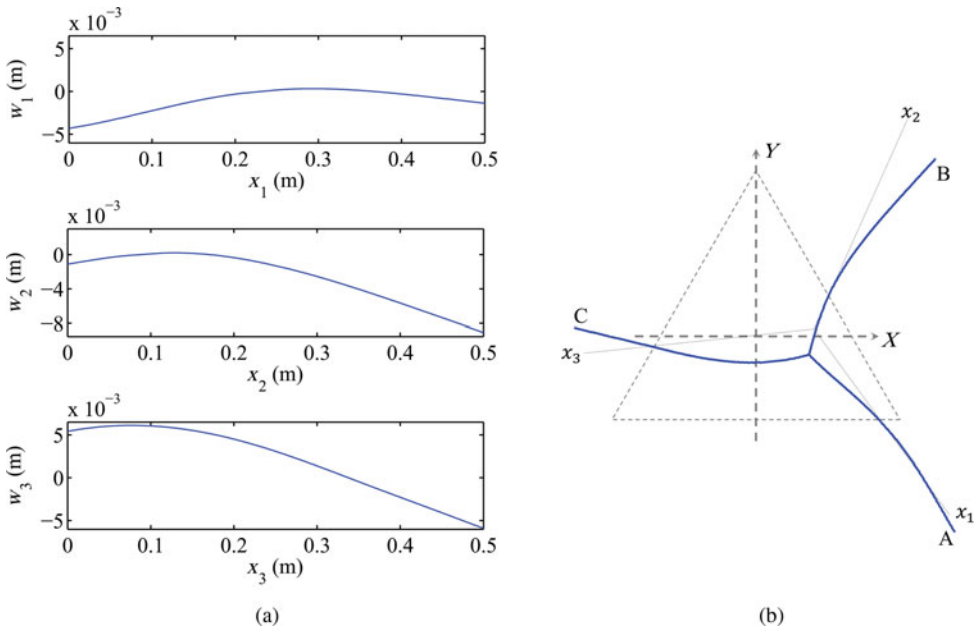


Fig. 18. Case study 3: beam shapes at $t = 0.5$ s; deformation axis is magnified: (a) elastic deformation of beams; (b) approximate rigid and elastic displacement of the star.

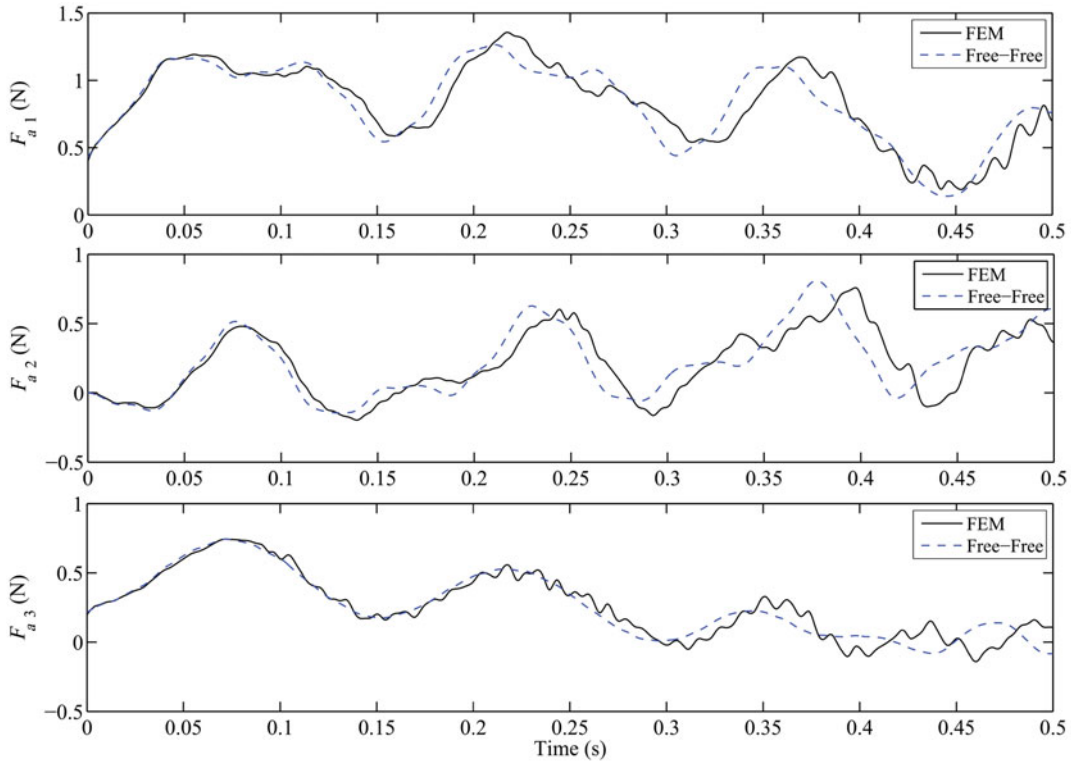


Fig. 19. Case study 3: amount of the three driving forces using free-free mode shapes.

The deformed shape of the moving platform obtained at $t = 0.5$ s using the slide-free mode shapes is shown in Fig. 22 for the case study 4. As expected, due to symmetrical motion along x_3-axis, the deformation of beams 1 and 2 are identical, while deformation of beam 3 is zero. Amount of the driving forces, F_{ai}, obtained using the slide-free mode shapes, are shown in Fig. 23.

https://doi.org/10.1017/S0263574714001398 Published online by Cambridge University Press

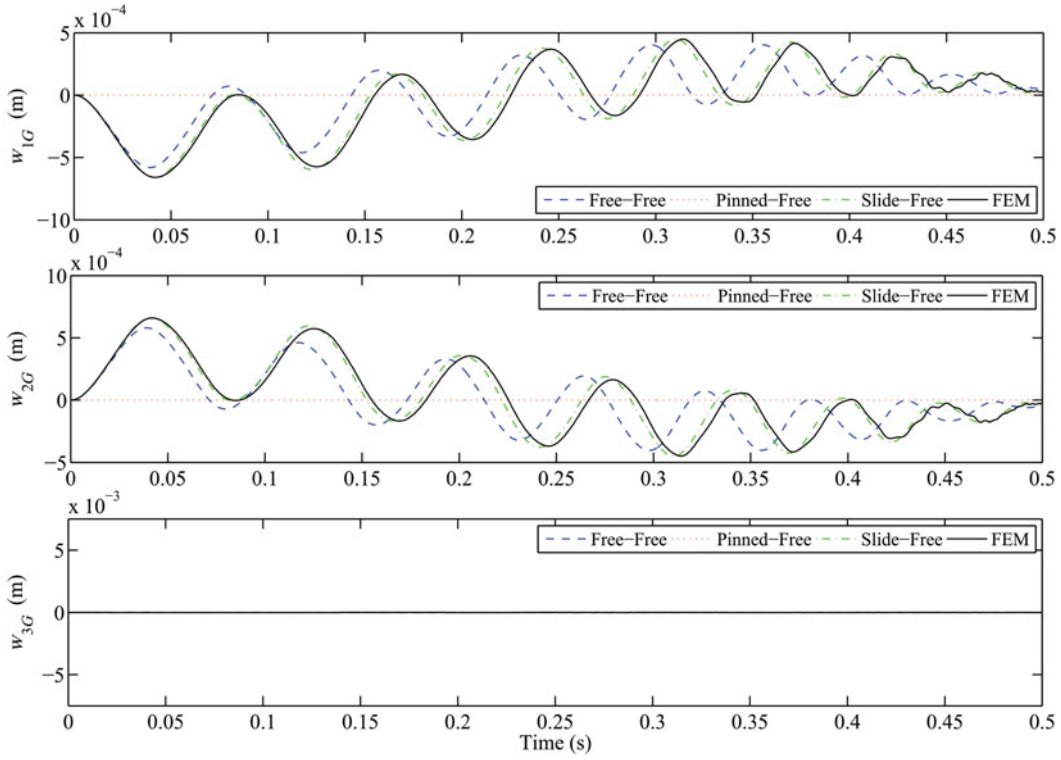


Fig. 20. Case study 4: elastic displacement of point G measured in the rigid body coordinate systems x_1w_1, x_2w_2, and x_3w_3.

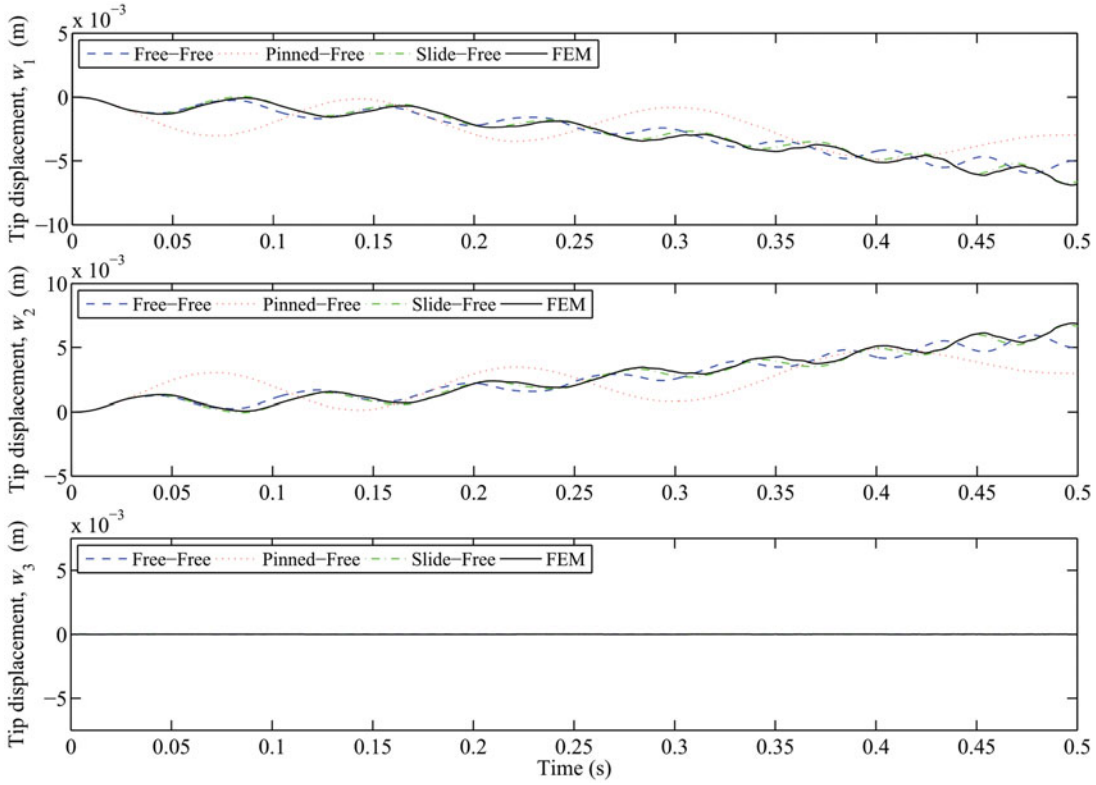


Fig. 21. Case study 4: elastic tip displacements for three beams measured in the rigid body coordinate systems x_1w_1, x_2w_2, and x_3w_3.

https://doi.org/10.1017/S0263574714001398 Published online by Cambridge University Press

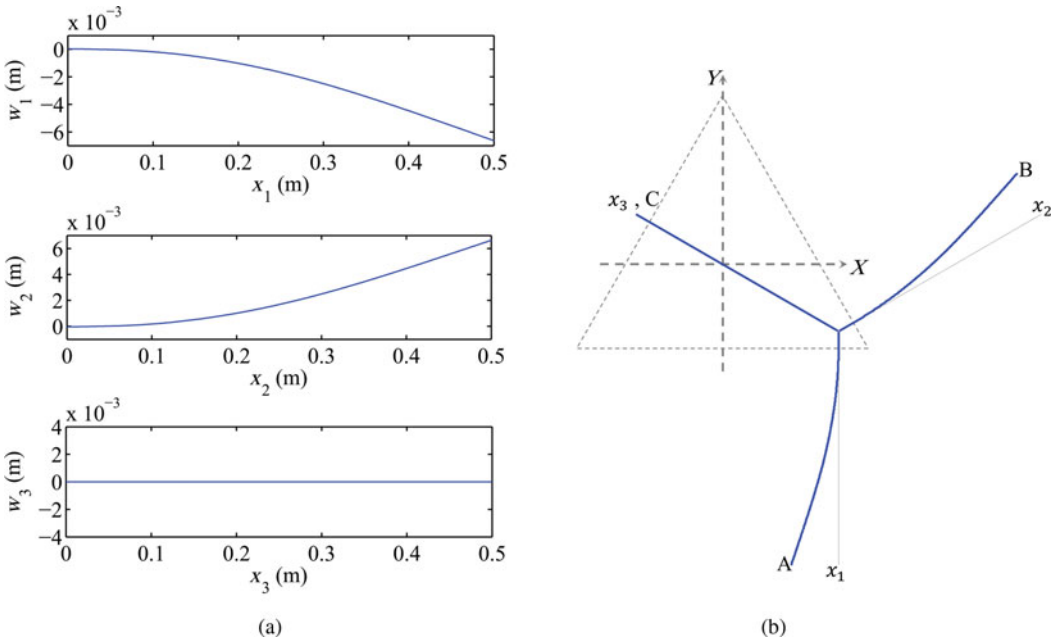


Fig. 22. Case study 4: beam shapes at $t = 0.5$ s; deformation axis is magnified: (a) elastic deformation of beams; (b) approximate rigid and elastic displacement of the star.

9. Discussion on Mode Shape Selection

The assumed mode method offers simplicity in solving the motion equation. The AMM typically assumes that one has some qualitative knowledge of the general behavior of the system deformations and boundary conditions. This knowledge helps to better select type of mode shapes. However, in the case of the ST parallel robot with an end-effector made up of three flexible beams, it is difficult to provide a qualitative assessment of the deflections of the point G. Therefore, it is difficult to select the right mode shape. Additionally, the choice of mode shapes should be taken with care as it depends on both how one has developed the model as well as type of motion of the robot. Therefore, in this paper in addition to test the correctness of the analytical model and its solution, we were motivated to also investigate the effect of different mode shapes on the accuracy of the solution.

The goal of the present paper is to obtain both the analytical model and solution for a parallel robot having a flexible platform with passive prismatic joints. To test the correctness of the analytical model and its solution, as well as accuracy of the solution, several trajectories each resulting in a unique type of motion were considered. Several mode shapes were tested for each of the trajectories. It is shown that for each trajectory, certain mode shapes produce better results. In order to make a quantitative comparison between the results obtained from the three different groups of assumed modes, an error variance parameter (EVP) is defined on the difference between the AMM results and the FEM results as follows:

$$\mathrm{EVP} = \frac{\int_0^{t_f} \left| \left(w_i^{\mathrm{AMM}}(x_0, t) - w_i^{\mathrm{FEM}}(x_0, t) \right) \right| \mathrm{d}t}{\int_0^{t_f} \left| w_i^{\mathrm{FEM}}(x_0, t) \right| dt} \times 100\%, \tag{45}$$

in which $w_i^{\mathrm{AMM}}(x_0, t)$ and $w_i^{\mathrm{FEM}}(x_0, t)$ are transverse vibrations obtained by AMM and FEM for point $x_i = x_0$, respectively. t_f is the simulation time. For each of the four case studies and each of the three groups of assumed modes, the EVP is calculated at points A, B, C, and G. Next, the average of the EVPs for points A, B, C, and G is calculated as a quantitative criterion. This quantity may be viewed to represent the accuracy of the selected assumed modes of the solution method for each case study. Results are summarized in Table I.

It is clear that all the three groups of mode shapes satisfy boundary conditions of the tip points, A, B, and C but differ at boundary conditions for point G. Note that satisfying the geometrical boundary

https://doi.org/10.1017/S0263574714001398 Published online by Cambridge University Press

Table I. Effect of selecting different mode shapes on the correctness and accuracy of the analytical solution.

	Motion type	Actual behavior of point G	Forced behavior for points A/B/C/G		
			Pinned-free	Slide-free	Free-free
			Correctness & best accuracy Error Variance Parameter (%)		
Case study 1	In place rotation	**Pinned behavior** $\begin{cases} w_i(0,t)=0 \\ \partial w_i/\partial x_i(0,t)\neq 0 \\ \partial^2 w_i/\partial x_i^2(0,t)=0 \\ \partial^3 w_i/\partial x_i^3(0,t)=0 \end{cases}$	✓&✓ 4.11%	✓&× 33.46%	✓&✓ 4.61%
Case study 2	Rectilinear translational	**General behavior** $\begin{cases} w_i(0,t)\neq 0 \\ \partial w_i/\partial x_i(0,t)\approx 0 \\ \partial^2 w_i/\partial x_i^2(0,t)\neq 0 \\ \partial^3 w_i/\partial x_i^3(0,t)\neq 0 \end{cases}$	×&× 125.57%	✓&✓ 22.50%	✓&× 32.21%
Case study 3	General plane motion	**General behavior** $\begin{cases} w_i(0,t)\neq 0 \\ \partial w_i/\partial x_i(0,t)\neq 0 \\ \partial^2 w_i/\partial x_i^2(0,t)\neq 0 \\ \partial^3 w_i/\partial x_i^3(0,t)\neq 0 \end{cases}$	×&× 74.61%	×&× 55.76%	✓&✓ 24.22%
Case study 4	Rectilinear translational	**Slide behavior** $\begin{cases} w_i(0,t)\neq 0 \\ \partial w_i/\partial x_i(0,t)=0 \\ \partial^2 w_i/\partial x_i^2(0,t)\neq 0 \\ \partial^3 w_i/\partial x_i^3(0,t)\neq 0 \end{cases}$	×&× 74.61%	✓&✓ 55.76%	✓&× 24.22%

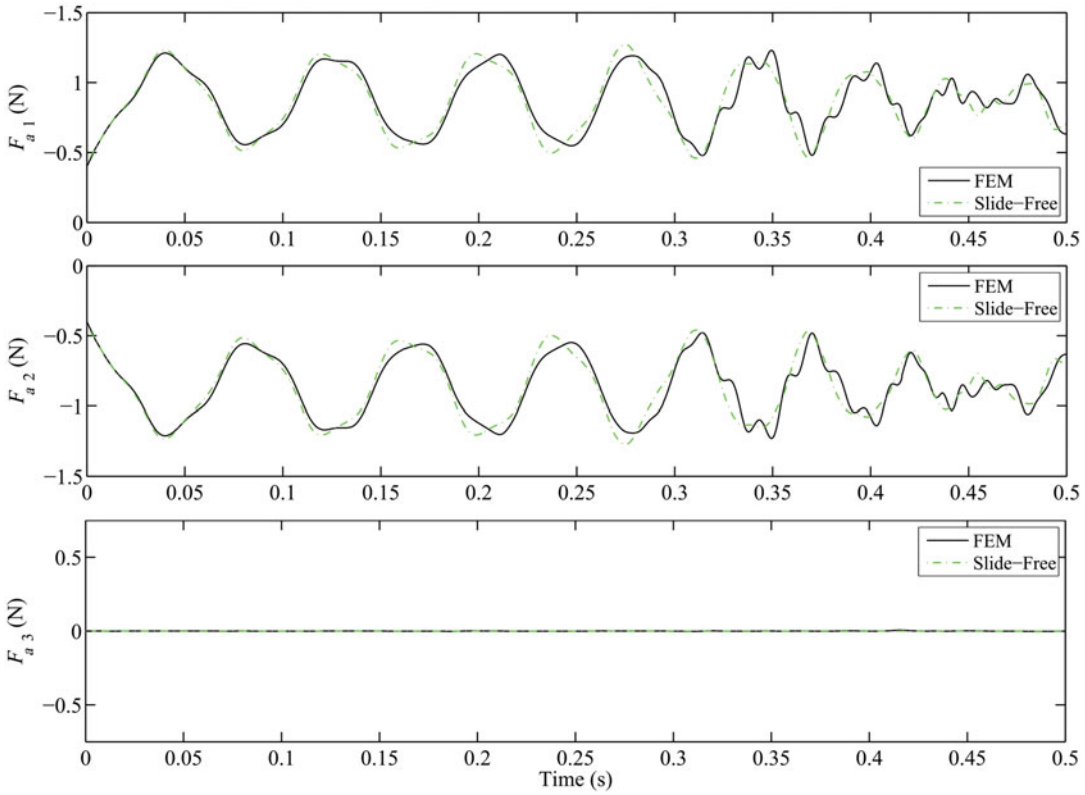


Fig. 23. Case study 4: amount of the three driving forces using slide-free mode shapes.

https://doi.org/10.1017/S0263574714001398 Published online by Cambridge University Press

conditions, $w_i(0,t)$ and $\partial w_i/\partial x_i(0,t)$, is more important than the natural boundary conditions, $\partial^2 w_i/\partial x_i^2(0,t)$ and $\partial^3 w_i/\partial x_i^3(0,t)$. Additionally, between the two natural boundary conditions, the second derivative is more important to satisfy than the third derivative.

In case study 1, motion of the star is symmetrical about origin O, therefore point G has a specific pinned behavior in which $w_i(0,t) = 0, \partial w_i/\partial x_i(0,t) \neq 0, \partial^2 w_i/\partial x_i^2(0,t) = 0$, and $\partial^3 w_i/\partial x_i^3(0,t) = 0$. Therefore, the pinned-free mode shapes which satisfy the geometrical boundary conditions at point G achieve the best accuracy. However, the free-free mode shapes satisfy the natural boundary conditions at point G. By applying the constraint equations of point G, in Section 4, the free-free mode shapes can be combined so as to satisfy the geometrical boundary conditions at point G. Therefore, the free-free mode shapes can also achieve the same accuracy of the pinned-free mode shapes. Note that because the slope of the slide-free mode shapes at point $x_i = 0$ is zero, any combination of the slide-free mode shapes cannot satisfy the non-zero slope condition at point G. Therefore, the slide-free mode shapes cannot satisfy the geometrical boundary conditions at point G resulting in a less accurate solution.

In case study 2, motion of the star is rectilinear translation and point G moves along X axis causing point G to have a sliding behavior in which $w_i(0,t) \neq 0, \partial w_i/\partial x_i(0,t) \approx 0, \partial^2 w_i/\partial x_i^2(0,t) \neq 0$, and $\partial^3 w_i/\partial x_i^3(0,t) \neq 0$. Therefore, the slide-free mode shapes which satisfy the geometrical boundary conditions at point G produce more accurate results. Also, note that the free-free mode shapes have produced correct but inaccurate results. This is because, applying the constraint equations of point G, in Section 4, allow the free-free mode shapes to be combined and satisfy the geometrical boundary conditions at point G. However, the free-free mode shapes do not satisfy the natural boundary conditions at point G. This is because both the natural boundary conditions of the free-free mode shapes as well as any of their combinations at point $x_i = 0$ are zero while in actuality natural boundary conditions at point G are non-zero. Therefore, the free-free mode shapes do not produce as much accuracy as the slide-free mode shapes.

In case study 3, the motion is symmetric neither about G nor about any of the x_i axis. This causes point G to have a general behavior in which all boundary conditions are generally non-zero. Therefore, the used pinned-free and slide-free mode shapes induced incorrect geometrical boundary condition at point G. Additionally, these two groups of mode shapes have zero geometrical boundary conditions at point $x_i = 0$, point G. Therefore, any combination of the pinned-free or slide-free mode shapes cannot meet the required non-zero geometrical boundary conditions at point G. As a result, these two groups of mode shapes do not produce an accurate solution for case study 3. In case study 3, the free-free mode shapes induced incorrect natural boundary conditions. However, what is more important is that they did not induce an incorrect geometrical boundary condition and therefore achieve a more accurate response.

In case study 4, motion of the star is symmetrical about x_3 axis. This results point G to have a slide behavior at x_3 direction in which for beam 1 and 2 we have $w_i(0,t) \neq 0, \partial w_i/\partial x_i(0,t) = 0, \partial^2 w_i/\partial x_i^2(0,t) \neq 0$, and $\partial^3 w_i/\partial x_i^3(0,t) \neq 0$. Considering the similarities between the boundary conditions between case study 2 and case study 4, we find that slide-free mode shapes achieve a more accurate response.

The pure translational motion discussed in case 4 assumed the robot starts at the origin of the fixed coordinate system, point O, and moves along beam i, in x_i direction (Fig. 24(a)). Because of the resulting symmetrical motion, the vibration effect of the two other beams cancels each other and therefore beam i does not vibrate. This results in a sliding behavior for point G. If we have other translational motions, such as shown in Figs. 24(b) and 24(c), then point G will have behavior similar to sliding behavior. Therefore, for the all cases shown in Fig. 24, the slide-free mode shapes produce more accurate results compared with the other two groups of mode shapes.

Referring to the four case studies and the summary shown in Table I, we may conclude that the free-free mode shapes, except in one specific type of motion, achieve the most accurate results of the presented analytical model.

10. Conclusion

In the present study, an analytical model for dynamic and vibration analysis of a 3-PRP planar parallel robot with a flexible moving platform having passive prismatic joints was presented and solved

https://doi.org/10.1017/S0263574714001398 Published online by Cambridge University Press

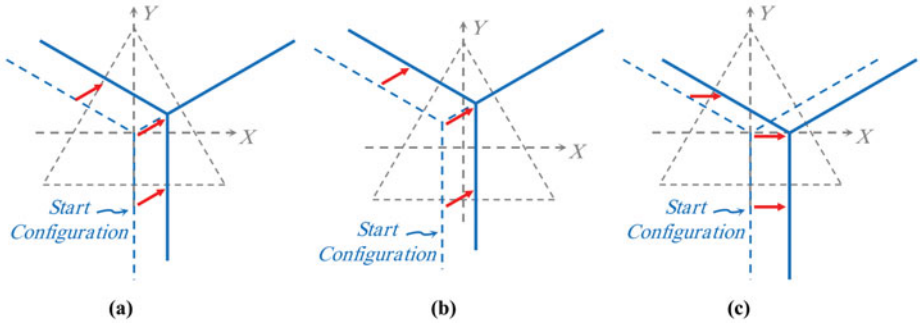


Fig. 24. Three types of translational motion of the star: (a) Case study 4: starts at origin *O* and moves along a beam; (b) does not start at origin *O* but moves along a beam; (c) Case study 2: starts at origin *O* but does not move along a beam.

using an approximate analytical method. First, the direct kinematics of the rigid robot as well as the acceleration due to elastic and rigid motion of an element of the moving platform was developed. Next, constraint equations for junction point of three flexible beams and prismatic joints were developed and used with previously developed motion equation of a single beam having a prismatic joint to obtain motion equations of the flexible moving platform. Constrained assumed modes method was used to obtain an approximate analytical solution. Using the Lagrange's multipliers, the generalized constraint forces were computed. Consequently, vibration of the robot and the inverse dynamic problem are simultaneously solved. The presented modeling can also be used to solve vibration of the robot along with direct dynamics problem. Additionally, the presented analytical model includes the effects of the mass, rotational inertia moment, and length of the prismatic joint.

Several motion trajectories of the robot, rotational, translational, and general planar motion, each inducing a different vibration behavior for the end-effector, were considered. Consequently, three different groups of mode shapes were investigated in the solution. It was shown that the free-free mode shapes resulted in better accuracy for all motions except a specific translational motion for which the slide-free mode shapes showed better results. Finally, to verify the analytical model and the solution, the robot was modeled using a commercial FEM software. It was shown that the analytical and the FEM software solutions closely followed each other.

The main contributions of this paper are: (1) presenting a method for vibration analysis of a 3-PRP planar parallel robot which can be simply extended to the robots having a flexible moving platform and passive prismatic joint(s); (2) obtaining analytical model and approximate analytical solution for vibrations of the ST parallel robot; (3) simultaneously solving the inverse/direct dynamics and vibration of the robot; (4) including effects of the passive prismatic joint parameters such as mass, rotational moment of inertia and the actual length in an analytical model for vibration of a parallel robot; (5) investigating the effect of assumed mode shapes on the accuracy of the analytical solution.

References

1. A. Fattah, J. Angeles and A. K. Misra, "Direct Kinematics of a 3-DOF Spatial Parallel Manipulator with Flexible Legs," *Proceedings of the 23rd ASME Mechanisms Conference*, Minneapolis, USA (Sep. 11–14, 1994), vol. 72, pp. 285–291.
2. A. Fattah, J. Angeles and A. K. Misra, "Dynamics of a 3-DOF Spatial Parallel Manipulator with Flexible Links," *Proceedings of the IEEE International Conference on Robotics and Automation*, Nagoya, Japan (May 21–27, 1995) Vol. 1, pp. 627–632.
3. A. Fattah, A. K. Misra and J. Angeles, "Dynamics of a Flexible-Link Planar Parallel Manipulator in Cartesian Space," *Proceedings of the 20th ASME Design Automation Conference*, Minneapolis, USA (Sep. 11–14, 1994), vol. 69(2), pp. 483–490.
4. G. Piras, W. L. Cleghorn and J. K. Mills, "Dynamic finite-element analysis of a planar high-speed, high-precision parallel manipulator with flexible links," *Mech. Mach. Theory* **40**, 849–862 (2005).
5. X. Wang and J. K. Mills, "Dynamic modeling of a flexible-link planar parallel platform using a substructuring approach," *Mech. Mach. Theory* **41**, 671–687 (2006).
6. D. Zhaocai and Y. Yueqing, "Dynamic modeling and inverse dynamic analysis of flexible parallel robots," *Int. J. Adv. Robot. Syst.* **5**(1), 115–122 (2008).
7. Z. Zhou, J. Xi and C. K. Mechefske, "Modeling of a fully flexible 3-PRS manipulator for vibration analsysis," *J Mech. Des.* **128**, 403–412 (2006).

https://doi.org/10.1017/S0263574714001398 Published online by Cambridge University Press

8. L. Shan-zeng, Y. Yue-qing, Z. Zhen-cai, S. Li-ying and L. Qing-bo, "Dynamic modeling and analysis of 3-RRS parallel manipulator with flexible links," *J. Cent. South Univ. Technol.* **17**, 323–331 (2010).
9. B. Kang and J. K. Mills, "Dynamic modeling of structurally-flexible planar parallel manipulator," *Robotica* **20**, 329–339 (2002).
10. X. Zhang, J. K. Mills and W. L. Cleghorn, "Vibration control of elastodynamic response of a 3-PRR flexible parallel manipulator using PZT transducers," *Robotica* **26**, 655–665 (2008).
11. M. Giovagnoni, "Dynamics of Flexible Closed-chain Manipulator," *Proceedings of the ASME Design Technical Conference*, Scottsdale, USA (1992), vol. 69(2), pp. 483–490.
12. J. D. Lee and Z. Geng, "Dynamic model of a flexible Stewart platform," *Comput. Struct.* **48**(3) 367–374 (1993).
13. S. K. Dwivedy and P. Eberhard, "Dynamic analysis of flexible manipulators, a literature review," *Mech. Mach. Theory* **41**, 749–777 (2006).
14. M. Sharifnia and A. Akbarzadeh, "An Analytical Model for Vibration and Control of a PR-PRP Parallel Robot with Flexible Platform and Prismatic Joint," *Journal of Vibration and Control*, Published online before print, 2 April 2014, doi: 10.1177/1077546314528966.
15. M. Sharifnia and A. Akbarzadeh, "Dynamics and Vibration of a 3-PSP Parallel Robot with Flexible Moving Platform," *Accepted for publication, Journal of Vibration and Control*.
16. A. Ibrahimbegovic and S. Mamouri, "On rigid components and joint constraints in nonlinear dynamics of flexible multibody systems employing 3D geometrically exact beam model," *Comput. Methods Appl. Mech.Eng.* **188**, 805–831 (2000).
17. O. A. Bauchau, "On the modeling of prismatic joints in flexible multi-body systems," *Comput. Methods Appl. Mech. Eng.* **181**, 87–105 (2000).
18. E. D. Stoenescu and D. B. Marghitu, "Effect of prismatic joint inertia on dynamics of kinematic chains," *Mech. Mach. Theory* **39**, 431–443 (2004).
19. H. R. Mohammadi Daniali, P. J. Zsombor-Murray and J. Angeles, "The Kinematics of 3-DOF Planar and Spherical Double-Triangular Parallel Manipulators," **In**: *Computational Kinematics* edited by J. Angeles, G. Hommel, and P. Kovacs, Kluwer Academic Publishers, Dordrecht, The Netherlands, pp. 153–164 (1993).
20. S. Ronchi, O. Company, F. Pierrot and A. Fournier, "PRP Planar Parallel Mechanism in Configurations Improving Displacement Resolution," *Proceedings of the 1st International Conference on Positioning Technology*, Hamamatsu, Japan (Jun. 9–11, 2004), pp. 279–284.
21. A. Taghvaeipour, J. Angeles and L. Lessard, "On the elastostatic analysis of mechanical systems," *Mech. Mach. Theory* **58**, 202–216 (2012).
22. R. Vidoni, A. Gasparetto and M. Giovagnoni, "Design and implementation of an ERLS-based 3-D dynamic formulation for flexible-link robots," *Robot. Comput.-Integr. Manuf.* **29**(2), 273–282 (2013).
23. M. Mosayebi, M. Ghayour and M. J. Sadigh, "A nonlinear high gain observer based input-output control of flexible link manipulator," *Mech. Res. Commun.* **45**, 34–41 (2012).
24. P. Staufer and H. Gattringer, "State estimation on flexible robots using accelerometers and angular rate sensors," *Mechatronics* **22**(8), 1043–1049 (2012).
25. M. A. Dokainish and R. Kumar, "Experimental and theoretical analysis of the transverse vibrations of a beam having bilinear support," *Exp. Mech.* **11**(6), 263–270 (1971).

https://doi.org/10.1017/S0263574714001398 Published online by Cambridge University Press